



The HI velocity function: a test of cosmology or baryon physics?

Garima Chauhan^{1,2}★ Claudia del P. Lagos^{1,2}★ Danail Obreschkow^{1,2}
 Chris Power^{1,2}★ Kyle Oman³ and Pascal J. Elahi^{1,2}

¹International Centre for Radio Astronomy Research (ICRAR), 7 Fairway, Crawley, WA 6009, Australia

²ARC Centre of Excellence for All Sky Astrophysics in 3 Dimensions (ASTRO 3D), Australia

³Kapteyn Institute, Landleven 12, NL-9747 AD Groningen, the Netherlands

Accepted 2019 July 11. Received 2019 July 3; in original form 2019 April 18

ABSTRACT

Accurately predicting the shape of the HI velocity function (VF) of galaxies is regarded widely as a fundamental test of any viable dark matter model. Straightforward analyses of cosmological N -body simulations imply that the Λ cold dark matter (Λ CDM) model predicts an overabundance of low circular velocity galaxies when compared to observed HI VFs. More nuanced analyses that account for the relationship between galaxies and their host haloes suggest that how we model the influence of baryonic processes has a significant impact on HI VF predictions. We explore this in detail by modelling HI emission lines of galaxies in the SHARK semi-analytic galaxy formation model, built on the SURFS suite of Λ CDM N -body simulations. We create a simulated ALFALFA survey, in which we apply the survey selection function and account for effects such as beam confusion, and compare simulated and observed HI velocity width distributions, finding differences of $\lesssim 50$ per cent, orders of magnitude smaller than the discrepancies reported in the past. This is a direct consequence of our careful treatment of survey selection effects and, importantly, how we model the relationship between galaxy and halo circular velocity – the HI mass–maximum circular velocity relation of galaxies is characterized by a large scatter. These biases are complex enough that building a VF from the observed HI linewidths cannot be done reliably.

Key words: galaxies: evolution – galaxies: formation – galaxies: kinematics and dynamics.

1 INTRODUCTION

The Λ cold dark matter (hereafter Λ CDM) model is well established as the Standard Cosmological Model, naturally predicting the structure of our Universe on intermediate-to-large scales and explaining a swathe of observational data, from the formation and evolution of large-scale structure, to the state of the Early Universe, to the cosmic abundance of different types of matter (e.g. Bull et al. 2016).

Despite its numerous successes, however, the Λ CDM model faces a number of challenges on small scales. Cold dark matter (hereafter CDM) haloes form cuspy profiles (i.e. the dark matter density rises steeply at small radii, Navarro, Frenk & White 1995), whereas observational inferences suggest that low-mass dark matter (hereafter DM) dominated galaxies have constant-density DM cores (Duffy et al. 2010; Oman et al. 2015; Dutton et al. 2018), leading to the so-called ‘cusp–core’ problem. CDM haloes are also predicted to host thousands of subhaloes, which has led to the conclusion that

the Milky Way (MW) suffers from a ‘missing satellites’ problem because it should host many more satellite galaxies than the ~ 50 that are observed (Bullock & Boylan-Kolchin 2017). While the inefficiency of galaxy formation in low-mass haloes – because of feedback processes such as e.g. cosmological reionization, supernovae, etc. – may lead to many subhaloes to be free of baryons and dark, the ‘too big to fail’ problem (Boylan-Kolchin, Bullock & Kaplinghat 2011) suggests that the central density of CDM subhaloes are too high; in dissipationless Λ CDM simulations of MW mass haloes, the most massive subhaloes, which are large enough to host galaxy formation and so ‘too big to fail’, have typical circular velocities 1.5 times higher ($\sim 30 \text{ km s}^{-1}$) than that observed at the half-light radii of the MW satellite. This indicates that there are problems with both the predicted abundances and internal structures of CDM subhaloes (Dutton et al. 2016).

Interestingly, with the emergence of observational surveys sensitive enough to detect statistical samples of faint galaxies in the nearby Universe, it has become clear that there is a consistent deficit in the observed abundance of low-mass galaxies when compared to predictions from the Λ CDM model (e.g. Tollerud et al. 2008; Hargis, Willman & Peter 2014). This suggests that the ‘missing satellite’ problem is more generically a ‘missing dwarf galaxy’

* E-mail: garima.chauhan@research.uwa.edu.au (GC);
claudia.lagos@uwa.edu.au (CPL); chris.power@uwa.edu.au (CP)

problem. This is most evident in measurements of the velocity function (VF) – the abundance of galaxies as a function of their circular velocity. The observed VF is assumed to be equivalent to the VF of DM subhaloes (Gonzalez et al. 2000), and so its measurement should provide a potentially powerful test of the Standard Cosmological Model.

The utility of the VF as a test of DM is already evident in the results of the $\text{H}\alpha$ VF measured by ALFALFA (The Arecibo Legacy Fast ALFA, Giovanelli et al. 2005); focusing on galaxies with rotational velocities of $\sim 25 \text{ km s}^{-1}$, the ALFALFA VF found approximately an order of magnitude fewer galaxies than expected from cosmological CDM simulations (Klypin et al. 2014; Brooks et al. 2017). Trujillo-Gomez et al. (2018) attempted to correct the measured $\text{H}\alpha$ velocities by including the effects of pressure support and derive a steeper VF, though still shallower than the ΛCDM prediction. This has prompted interest in warm dark matter (hereafter WDM) models, which predict significantly less substructure within haloes (Maccio et al. 2012; Zavala et al. 2009). The linear matter power spectrum in WDM cosmologies is characterized by a steep cutoff at dwarf galaxy scales, which results in the suppression of low-mass structure formation and a reduction in the number of dwarf galaxies such that the VF predicted by the WDM model is more consistent with observations (Schneider et al. 2012). While the WDM model has the potential to provide a better description of the observed VF, there is a tension between the range of WDM particle masses required ($< 1.5 \text{ keV}$; cf. Schneider et al. 2017) and independent observational constraints from the Lyman- α forest at high redshifts, which rule out such low WDM particle masses (Klypin et al. 2014).

An alternative solution that has been recently discussed to alleviate the discrepancy between the observed and predicted VF is the effect of baryonic physics. Brooks et al. (2017) and Maccio et al. (2016) used cosmological zoom-in hydrodynamical simulations of a small number of galaxies (typically ranging from 30 to 100) to produce $\text{H}\alpha$ emission lines for their galaxies. They measured W_{50} (width of the $\text{H}\alpha$ emission line at 50 per cent of the maximum peak flux), which is used as a proxy in observations to estimate the $\text{H}\alpha$ velocity of the galaxy, and then compared them with the rotational velocity, V_{DMO} , of the haloes from the dark matter only (DMO) simulations. They found that due to the effect of baryons, W_{50} and V_{DMO} are non-linearly correlated, in a way that W_{50} tends to underestimate V_{DMO} in low-mass haloes, while the opposite happens at the high-mass end. They propose that a DM density profile that varies with stellar-to-halo mass ratio can be used to reconcile the differences with the observations. Trujillo-Gomez et al. (2018), however, showed that including the feedback-induced deviations from the ΛCDM VF predicted by the hydrodynamical simulations above were insufficient to reproduce the observed VF.

Although the work of Brooks et al. (2017) and Maccio et al. (2016) present a compelling solution to the apparent missing dwarf galaxy problem, their sample is statistically limited. Obreschkow et al. (2013) approached this problem from a different perspective, with much better statistics (going into a million of simulated galaxies). They attempted to see how the selection biases of the surveys might contribute to this problem. Their solution was to make a mock survey using DMO N -body simulations combined with semi-analytic models of galaxy formation, and then compare its results with the actual observations via producing a light-cone (see Section 2.1) with all the required selection effects. They did this for the HIPASS survey ($\text{H}\alpha$ Parkes All-Sky Survey, Meyer et al. 2004), as their simulation was limited in resolution to moderate halo masses, and hence was more directly comparable to HIPASS.

HIPASS is the first blind $\text{H}\alpha$ survey in the Southern hemisphere with a velocity range of -1280 to 12700 km s^{-1} , identifying over 5317 $\text{H}\alpha$ sources in total (including both Northern and Southern hemispheres). Obreschkow et al. (2013) found that the observed $\text{H}\alpha$ linewidths were consistent with ΛCDM at the resolution of the Millennium simulation (Springel et al. 2005), though they could not comment on haloes of lower mass, in which the largest discrepancies have been reported.

The main limitations of the works above have been either statistics or limited resolution. Here, we approach this problem with the SURFS suite (Elahi et al. 2018) of N -body simulations, which covers a very large dynamic range, from circular velocities of 20 to $> 500 \text{ km s}^{-1}$, and combine it with the state-of-the-art semi-analytic model SHARK (Lagos et al. 2018), which includes a sophisticated multiphase interstellar medium modelling. We use these new simulations and model to build upon the work of Obreschkow et al. (2013), and present a thorough comparison with the 100 per cent data release of ALFALFA (Haynes et al. 2018). We focus on the ALFALFA survey as it is a blind $\text{H}\alpha$ survey and covers a greater cosmological volume with a better velocity and spatial resolution than other previous $\text{H}\alpha$ surveys. We show that our simulated ALFALFA light-cone produces a W_{50} distribution in very good agreement with the observations, even down to the smallest galaxies detected by ALFALFA, and discuss the physics behind these results and their implications.

This paper is organized as follows. Section 2 describes the galaxy formation model used in this study and the construction of the mock ALFALFA survey. In Section 3, the modelling of the $\text{H}\alpha$ emission lines is described along with its application on the mock-sky built in the previous section. Section 4, we compare our results with ALFALFA observations and discuss our results in the context of previous work. Section 5 summarizes our main results. In Appendix A, we compare our model for the $\text{H}\alpha$ emission line of galaxies with the more complex $\text{H}\alpha$ emission lines obtained from the cosmological hydrodynamical simulations APOSTLE (Oman et al. 2019).

2 THE SIMULATED GALAXY CATALOGUE

Our simulated galaxy catalogue is constructed using the SHARK semi-analytic model (Lagos et al. 2018) that was run on the SURFS N -body simulations suite (Elahi et al. 2018). Here, we describe briefly SHARK and SURFS.

Hierarchical galaxy formation models, such as SHARK, require three basic pieces of information about DM haloes : (i) the abundance of haloes of different masses; (ii) the formation history of each halo; and in some cases (iii) the internal structure of the halo including their radial density and their angular momentum (Baugh 2006). These fundamental properties are now well established, thanks to the N -body simulations like SURFS (used in this study).

The SURFS suite consists of N -body simulations of differing volumes, from 40 to $210 h^{-1} \text{ cMpc}$ on a side, and particle numbers, from ~ 130 million up to ~ 8.5 billion particles, using the ΛCDM *Planck* cosmology (Planck Collaboration XIII 2016). The latter has a total matter, baryon, and dark energy densities of $\Omega_m = 0.3121$, $\Omega_b = 0.0491$ and $\Omega_L = 0.6751$, and a dimensionless Hubble parameter of $h = 0.67512$. The SURFS suite is able to resolve DM haloes down to $8.3 \times 10^8 h^{-1} \text{ M}_\odot$. For this analysis, we use the L40N512 and L210N1536 runs, referred to as micro-SURFS and medi-SURFS respectively hereafter, whose properties are given in Table 1. Merger trees and halo catalogues were constructed using the phase-space finder VELOCIRAPTOR (Elahi et al. 2019a; Welker

Table 1. SURFS simulation parameters of the runs being used in this paper. We refer to L40N512 and L210N1536 as micro-SURFS and medi-SURFS, respectively.

Name	Box size $L_{\text{box}}(\text{cMpc } h^{-1})$	Number of particles, N_p	Particle mass $m_p(\text{M}_\odot h^{-1})$	Softening length $\epsilon(\text{kpc } h^{-1})$
L40N512	40	512 ³	4.13×10^7	2.6
L210N1536	210	1536 ³	2.21×10^8	4.5

et al. 2018) and the halo merger tree code TREEFROG (Poulton et al. 2018; Elahi et al. 2019b).

SHARK was introduced by Lagos et al. (2018), and is an open source, flexible, and highly modular cosmological semi-analytic model of galaxy formation, which is hosted in GitHub.¹ It models key physical processes that shape the formation and evolution of galaxies, including (i) the collapse and merging of DM haloes; (ii) the accretion of gas onto haloes, which is governed by the DM accretion rate; (iii) the shock heating and radiative cooling of gas inside DM haloes, leading to the formation of galactic discs via conservation of specific angular momentum of the cooling gas; (iv) the formation of a multiphase interstellar medium and star formation (SF) in galaxy discs; (v) the suppression of gas cooling due to photo-ionization; (vi) chemical enrichment of stars and gas; (vii) stellar feedback from the evolving stellar populations; (viii) the growth of supermassive black holes via gas accretion and merging with other black holes; (ix) heating by active galactic nuclei (AGNs); (x) galaxy mergers driven by dynamical friction within common DM haloes which can trigger bursts of SF and the formation and/or growth of spheroids; and (xi) the collapse of globally unstable discs that also lead to the bursts of SF and the formation and/or growth of bulges. SHARK includes several different models for gas cooling, AGN feedback, stellar and photo-ionization feedback, and SF. The model also numerically evolves the exchange of mass, metals, and angular momentum between the key gas reservoirs of haloes and galaxies: halo hot and cold gas, galaxy stellar and gaseous’ disc and bulge (and within discs between the atomic and molecular gas), central black hole, and the ejected gas component (outside haloes).

Halo gas in SHARK is assumed to be in two phases: cold, which is expected to cool within the duration of a halo’s dynamical time; and hot, which remains at the virial temperature of the halo. Cold gas is assumed to settle onto the disc and follows an exponential profile of half-mass radius $r_{\text{gas, disc}}$. In our model $r_{\text{gas, disc}}$ can differ from the stellar half-mass radius as stars form only from the molecular hydrogen (H_2) and not the total gas. Surface densities of H I and H_2 are calculated using the pressure relation of Blitz & Rosolowsky (2006), described in detail in Section 3.1.

Models and parameters used in this study are the defaults of SHARK as described in Lagos et al. (2018), which were calibrated to reproduce the $z = 0, 1$, and 2 stellar mass functions; the $z = 0$ black hole–bulge mass relation; and the disc and bulge mass–size relations. In addition, the model reproduces well observational results that are independent of those used in calibration, including the total neutral, atomic and molecular hydrogen–stellar mass scaling relations at $z = 0$; the cosmic star formation rate (SFR) density evolution up to $z \approx 4$; the cosmic density evolution of the atomic and molecular hydrogen at $z \lesssim 2$ or higher in the case of the latter; the mass–metallicity relations for the gas and stars; the contribution to the stellar mass by bulges and the SFR–stellar mass relation in the local Universe. Davies et al. (2018) show that SHARK

also reproduces the scatter around the main sequence of SF in the SFR–stellar mass plane, while Martindale et al. (in preparation) show that SHARK reproduces the H I content of groups as a function of halo mass. Of particular importance for this study is SHARK’s success in recovering the observed gas abundances of galaxies.

2.1 A mock ALFALFA sky

To ensure a fair comparison with available H I surveys, we first estimate how predicted galaxy properties are likely to be influenced by the choice of selection criterion. Here, mock galaxy catalogues are a particularly powerful tool, and so we begin by constructing a ‘mock ALFALFA’ survey. We do this by generating a galaxy population with SHARK and embed them within a cosmological volume by applying the survey’s angular and radial selection functions (e.g. Merson et al. 2013).

We use the code STINGRAY, which is an extended version of the light-cone of Obreschkow et al. (2009b), to build our light-cones from the SHARK outputs. Rather than forming a single chain of replicated simulation boxes, STINGRAY tiles boxes together to build a more complex 3D field along the line of sight of the observer. Galaxies are drawn from simulation boxes which correspond to the closest lookback time, which ranges over the redshift range $z = 0$ to 0.06 (corresponding to the ALFALFA limit); in the SHARK simulations, this corresponds to the last seven snapshots. Properties of each galaxy in the light-cone are obtained from the closest available time-step, resulting in the formation of spherical shells of identical redshifts. A possible issue would be the same galaxy appearing once in every box, but due to cosmic evolution might display different intrinsic properties. In order to avoid this problem, galaxy positions are randomized by applying a series of operations consisting of 90° rotations, inversions, and continuous translations. We build the light-cones with all the galaxies in SHARK that have a stellar or cold gas mass (atomic plus molecular) $\geq 10^6 \text{ M}_\odot$. Any additional selection (in this case the one specific to ALFALFA) are applied later, directly to the light-cone galaxies. The end result of the whole process is that we get a mock-observable sky as shown in Fig. 1 which is as near to the real sky as possible and with minimum repetition of the large-scale structure. The two portions of the sky shown correspond to the north and south ALFALFA regions.

STINGRAY also computes an inclination for each galaxy with respect to the observer. The latter are constructed assuming galaxies to have an angular momentum vector of the same direction as of its subhalo angular momentum vector (as measured by VELOCIRAPTOR), in the case of central galaxies and satellites galaxies type = 1. For type = 2 satellite galaxies, we assume random orientations. Satellites type = 1 correspond to those hosted by satellite subhaloes that are identified by VELOCIRAPTOR, while satellites type = 2 correspond to those that were hosted by subhaloes that have ceased to be identified by VELOCIRAPTOR. The latter usually happens when subhaloes become too low mass to be robustly identified (see Poulton et al. 2018 for a detailed analysis of satellite subhalo orbits). The overall effect of inclinations is to reduce W_{50} .

A limitation of any observational survey is finite velocity and spatial resolution, which for a survey like ALFALFA can lead to two or more galaxies falling inside the same beam and then overlapping in frequency, more commonly known as ‘beam confusion’. To mimic the effect of confusion in our analysis, we merge simulated galaxies whose centroids are separated by less than a projected 3.8 arcmin (the full-width-half-max for the ALFALFA beam) and whose H I lines overlap in frequency. In the case of galaxies being

¹<https://github.com/ICRAR/shark>

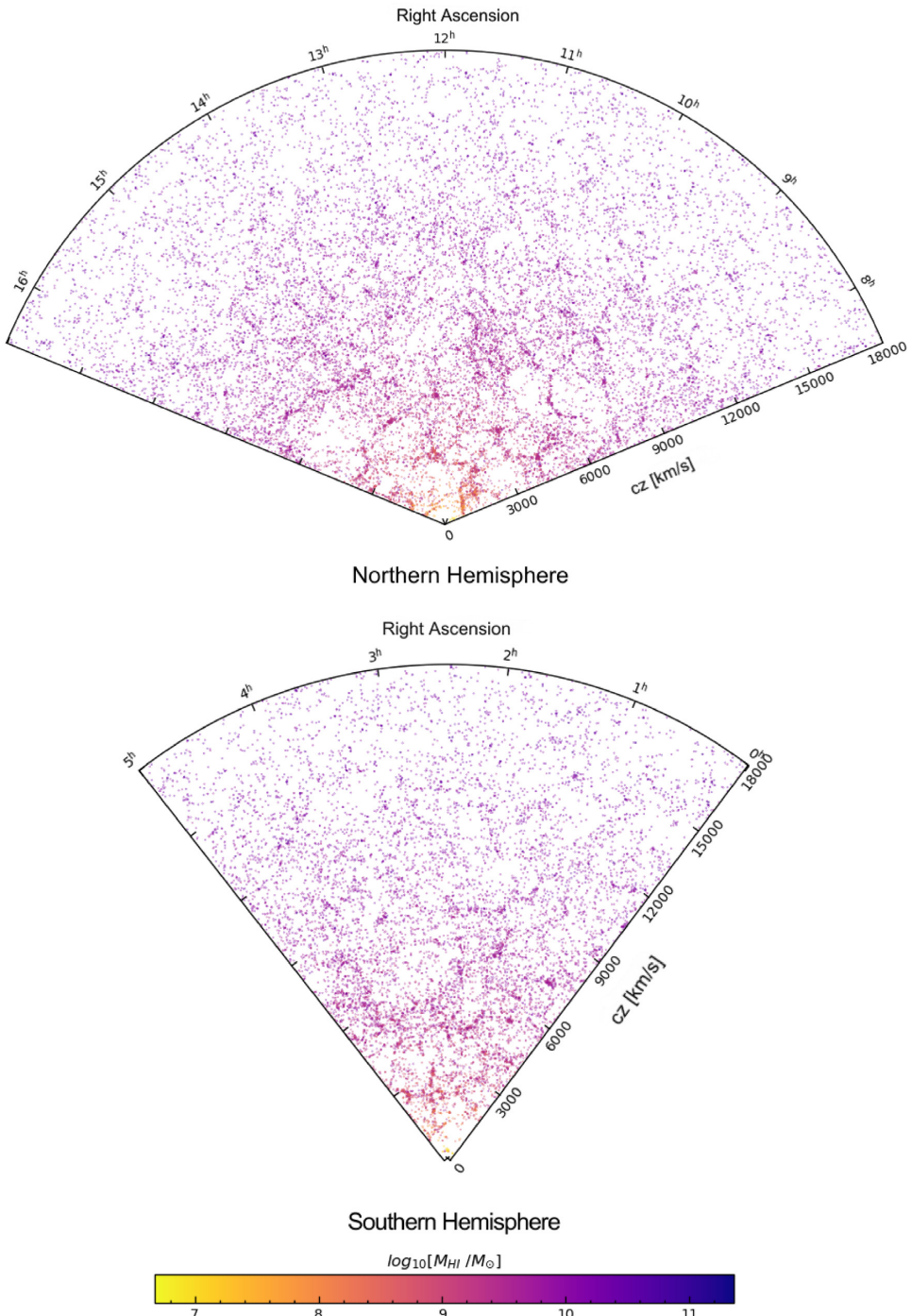


Figure 1. Mock sky of the ALFALFA survey, created with the outputs of SHARK and processed with STINGRAY to create the observable sky. Symbols show individual galaxies and colours show their $\text{H}\alpha$ mass, as labelled by the colour bar at the bottom. Low $\text{H}\alpha$ mass galaxies are only detected in the very nearby universe.

confused, the common $\text{H}\alpha$ mass is taken as the sum of the individual $\text{H}\alpha$ masses of the galaxies, and the W_{50} (the full-width at half of the peak flux of the line) is measured for the combined line formed due to the overlapping $\text{H}\alpha$ lines. Obreschkow et al. (2013) found that ‘confused’ galaxies typically have high $\text{H}\alpha$ mass and W_{50} , with $M_{\text{H}\alpha} > 10^{10} M_{\odot}$ and $W_{50} > 300 \text{ km s}^{-1}$, albeit for the HIPASS survey, which has a larger beam than ALFALFA; we find fewer confused galaxies lying in this range in our sample. By including

confusion, we reduce the total number of galaxies by <1 per cent, throughout the whole dynamical range of galaxies.

To ensure that we have the dynamical range in circular velocity in our sample of galaxies required to test the ‘missing satellite problem’, we make two light-cones using the micro- and medi-SURFS; micro-SURFS gives us better mass resolution to probe down to dwarf galaxies, with $M_{\text{H}\alpha} \lesssim 10^9 M_{\odot}$, while medi-SURFS provides us with a much larger volume and better statistics at the high-mass

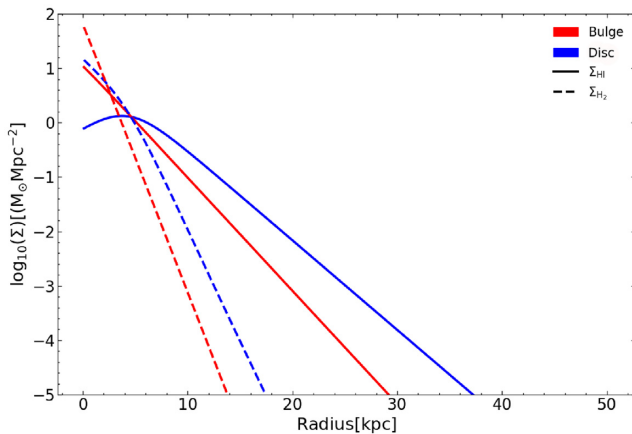


Figure 2. Surface density radial profiles of H₁ in the disc and bulge, as labelled, for an example SHARK galaxy, used to model the H₁ emission lines. The solid and dashed lines represent the H₁ and H₂ surface density of the galaxy, respectively. As it can be seen, there is a presence of H₁ in the bulge of the galaxy, which drops down steeply in the beginning, but the H₁ in the disc extends much further, and dominates beyond $\gtrsim 4$ kpc. There is a significant amount of H₂ present in the bulge, though it declines much more rapidly than the extended H₁ disc.

end, $M_{\text{HI}} \gtrsim 10^9 M_{\odot}$. Results for these light-cones are presented in Section 4.2.

3 MODELLING H₁ EMISSION LINES IN GALAXY FORMATION MODELS

In this section, we describe the steps required to build an H₁ emission line for each SHARK galaxy. Sections 3.1 and 3.2 provide details of the surface density and velocity profile calculations, respectively. The way we combine them to create the H₁ emission line is described in Section 3.3.

3.1 Gas mass and profile

For the calculation of the H₁ surface density profile, we adopt the empirical model described in Blitz & Rosolowsky (2004) and Blitz & Rosolowsky (2006, equation 1). In their model, the ratio of molecular to atomic hydrogen gas surface density in galaxies is a function of hydro-static pressure in the mid-plane of the disc, with a power-law index close to 1,

$$R_{\text{mol}}(r) = [P_{\text{ext}}(r)/P_{\star}]^{\alpha}, \quad (1)$$

where $R_{\text{mol}} \equiv \Sigma_{\text{H}_2}/\Sigma_{\text{H}_1}$, with Σ_{H_2} and Σ_{H_1} being the surface density of molecular and atomic hydrogen, respectively. The parameters P_{\star} and α are measured in observations, and in SHARK we adopt $P_{\star} = 34,673 \text{ K cm}^{-3}$ and $\alpha = 0.92$, which correspond to the best-fitting values in Blitz & Rosolowsky (2006).

Blitz & Rosolowsky (2006) adopted the Elmegreen (1989) estimate of P_{ext} for disc galaxies, which corresponds to the mid-plane pressure in an infinite, two-fluid disc with locally isothermal stellar and gas layers,

$$P_{\text{ext}}(r) = \frac{\pi}{2} G \Sigma_g \left[\Sigma_g + \left(\frac{\sigma_{\text{gas}}}{\sigma_{\star}} \right) \Sigma_{\star} \right], \quad (2)$$

where $P_{\text{ext}}(r)$ is the kinematic mid-plane pressure outside molecular clouds, and the input for equation (1). G is the gravitational constant, Σ_g is the total gas surface density (atomic plus molecular), Σ_{\star} is

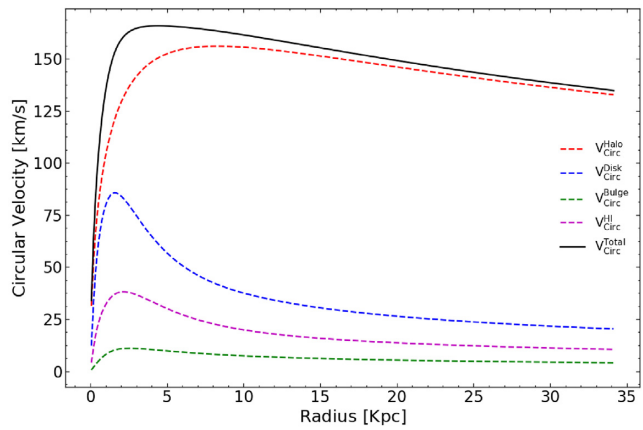


Figure 3. Radial circular velocity profile of the same galaxy showed in Fig. 2 (solid line), highlighting the contribution of all the components: stellar and gaseous disc, bulge and halo of the galaxy of, as labelled (see Section 3.2 for details). The velocity profile of this galaxy is dominated by DM at all radii.

the stellar surface density, and σ_{gas} and σ_{\star} are the gas and stellar vertical velocity dispersion, respectively.

The stellar and gas surface densities are assumed to follow exponential profiles with a half-gas and half-stellar mass radii of $r_{\text{gas, disc}}$ and $r_{\star, \text{disc}}$, respectively. We adopt $\sigma_{\text{gas}} = 10 \text{ km s}^{-1}$ (Leroy et al. 2008) and calculate $\sigma_{\star} = \sqrt{\pi G h_{\star} \Sigma_{\star}}$. Here, h_{\star} is the stellar scale height, and we adopt the observed relation $h_{\star} = r_{\star, \text{disc}}/7.3$ (Kregel, Van Der Kruit & Grijl 2002), with $r_{\star, \text{disc}}$ being the half-stellar mass radius.

Fig. 2 shows the radial surface density profile for an example galaxy in SHARK with a stellar and H₁ mass of 10^9 and $10^8 M_{\odot}$, respectively. The inner radius is dominated by H₂, with H₁ forming a core there. The latter is due to the saturation of H₁ at high column densities, above which the gas is converted into H₂. The sum of both gas components is exponential, however, the individual ones can deviate from that assumption. H₁ typically dominates at the outer radius.

Previous work by Obreschkow et al. (2009, 2013) assumed the total gas disc to have an exponential profile with a scale length that was larger than the stellar one by a factor >1 . They determined the H₁/H₂ ratio locally in post-processing using the Blitz & Rosolowsky (2006) model, with updated empirical parameters obtained from THINGS (The HI Nearby Galaxy Survey, Walter et al. 2008). Thus, our work improves on this by (i) allowing the H₁ to have a more complex profile, such as the example of Fig. 2, though still axisymmetric, and (ii) by calculating the multiphase nature of galaxies self-consistently within the galaxy formation calculation. The latter directly impacts galaxy evolution as stars can only form from molecular hydrogen in SHARK. In our model, H₁ can also exist in the bulges of galaxies, which in general allows the models to reproduce the observed gas content of early-type galaxies (Serra et al. 2010; Lagos et al. 2014, 2018).

3.2 Circular velocity profile

The circular velocity profiles are constructed following Obreschkow et al. (2009), which we briefly describe in this section. We assume a Navarro–Frenk–White (NFW; Navarro et al. 1995) halo radial profile, which describes the DM halo density profiles not as isothermal

(i.e. $\rho \propto r^{-2}$) but with a radially varying logarithmic slope

$$\rho_{\text{halo}}(r) = \rho_0 [(r/r_s)(1 + r/r_s)^2]^{-1}, \quad (3)$$

where ρ_0 is a normalization factor and r_s is the characteristic scale radius of the halo (where the profile has a logarithmic slope of -2). The virial radius, r_{vir} is calculated using the virial velocity of the haloes, V_{vir} , following the relation,

$$r_{\text{vir}} = \frac{GM_{\text{vir}}}{V_{\text{vir}}^2}, \quad (4)$$

where M_{vir} is the virial mass of the halo. Here, we define the virial mass as the mass enclosed within the halo when the overdensity is 200 times that of critical density. The scale radius, r_s , is defined as $r_s = r_{\text{vir}}/c_{\text{halo}}$, where c_{halo} is the concentration parameter, which in SHARK is estimated using the Duffy et al. (2008) relation.

For a spherical halo, the circular velocity profile will be $V_c^{\text{halo}2} = \frac{GM_{\text{halo}}(r)}{r}$, where $M_{\text{halo}}(r)$ is the mass enclosed within the radius r . Therefore, the circular velocity profile of the halo is,

$$V_c^{\text{halo}2}(x) = \left(\frac{GM_{\text{vir}}}{r_{\text{vir}}} \right) \times \frac{\ln(1 + c_{\text{halo}}x) - \frac{c_{\text{halo}}x}{1+c_{\text{halo}}x}}{x \left[\ln(1 + c_{\text{halo}}) - \frac{c_{\text{halo}}}{1+c_{\text{halo}}} \right]}, \quad (5)$$

where $x \equiv r/r_{\text{vir}}$. For larger radii, the circular halo velocity approaches the point mass velocity profile $V_c^{\text{halo}2} \approx GM_{\text{vir}}/r$.

For the velocity profile of the disc, we use the stellar and gas surface densities calculated with SHARKStellar and gas surface density profiles are assumed to follow an exponential form with a distinct half-mass radius for stellar and gas components. We calculate velocity profiles for stars and gas separately and then combine them to give V_c^{disc} . Following Obreschkow et al. (2009), we define the circular velocity for the stellar disc, $V_c^{*,\text{disc}}$, as

$$V_c^{*,\text{disc}2}(x) \approx \frac{G M^{*,\text{disc}}}{r_{\text{vir}}} \times \frac{c_{*,\text{disc}} + 4.8 c_{*,\text{disc}} \exp[-0.35 c_{*,\text{disc}} x - 3.5/(c_{*,\text{disc}} x)]}{c_{*,\text{disc}} x + (c_{*,\text{disc}} x)^{-2} + 2(c_{*,\text{disc}} x)^{-1/2}}, \quad (6)$$

where $c_{*,\text{disc}} \equiv r_{\text{vir}}/r_{s,\text{disc}}$ is the stellar disc concentration parameter, where $r_{s,\text{disc}} = r_{*,\text{disc}}/1.67$ is the scale radius of the stellar disc. $M^{*,\text{disc}}$ is the total mass of the stellar disc. We then calculate the contribution to the circular velocity from gas, V_c^{gas} , which we also describe as an exponential disc, and thus can be calculated as,

$$V_c^{\text{gas}2}(x) \approx \frac{GM^{\text{gas}}}{r_{\text{vir}}} \times \frac{c_{\text{gas}} + 4.8 c_{\text{gas}} \exp[-0.35 c_{\text{gas}} x - 3.5/(c_{\text{gas}} x)]}{c_{\text{gas}} x + (c_{\text{gas}} x)^{-2} + 2(c_{\text{gas}} x)^{-1/2}}, \quad (7)$$

where $c_{\text{gas}} \equiv r_{\text{vir}}/r_{s,\text{gas}}$ is the concentration parameter for the gas disc, where $r_{s,\text{gas}} = r_{\text{gas}}/1.67$. M^{gas} is the total cold gas mass (atomic plus molecular) of the galaxy.

We note that equations (6) and (7) are an approximate solution for an exponential profile provided by Obreschkow et al. (2009a). We describe bulges as spherical structures following a density profile according to the Plummer Model (Plummer 1911),

$$\rho_{\text{bulge}}(r) \approx \frac{3M^{\text{bulge}}}{4\pi r_{\text{Plummer}}^3} \left[1 + \left(\frac{r}{r_{\text{Plummer}}} \right)^2 \right]^{-5/2}, \quad (8)$$

with $r_{\text{Plummer}} \approx 1.7r_{\text{bulge}}$, and r_{bulge} is the half-mass radius of the bulge. The contribution to the total circular velocity profile by the

bulge is thus follows,

$$V_c^{\text{bulge}2}(x) = \frac{GM^{\text{bulge}}}{r_{\text{vir}}} \times \frac{(c_{\text{bulge}}x)^2 c_{\text{bulge}}}{[1 + (c_{\text{bulge}}x^2)]^{3/2}} \quad (9)$$

where $c_{\text{bulge}} \equiv r_{\text{vir}}/r_{s,\text{bulge}}$ is the bulge concentration parameter, where $r_{s,\text{bulge}} = r_{\text{bulge}}/1.67$. Unlike the V_c^{disc} calculation, where we calculate gas and stellar terms separately, we assume gas and stars within the bulge to follow the same profile with the same scale radius when computing V_c^{bulge} ; we combine their masses and calculate a single bulge contribution to the circular velocity profile. The latter was done as during the development of this model, we noted that the bulge gas and stellar radius were generally very similar and so we simply combined stellar and gas masses and used only the stellar bulge radius for our calculations.

Now that we have all our components calculated, we can estimate the total circular velocity profile, V_c as,

$$V_c^2(x) = V_c^{\text{halo}2}(x) + V_c^{*,\text{disc}2}(x) + V_c^{\text{gas}2}(x) + V_c^{\text{bulge}2}(x), \quad (10)$$

which we use to construct the $\text{H}\alpha$ emission-line profiles.

3.3 Emission-line profile

To construct the $\text{H}\alpha$ emission line associated with any circular velocity profile, we consider the line profile of a flat ring with constant circular velocity V_c and a normalized flux.

After imposing the normalization condition $\int dV_{\text{obs}} \tilde{\psi}(V_{\text{obs}}) \equiv 1$, the edge-on line profile of a ring is,

$$\tilde{\psi}(V_{\text{obs}}, V_c) = \begin{cases} \frac{1}{\pi\sqrt{V_c^2 - V_{\text{obs}}^2}} & \text{if } |V_{\text{obs}}| < V_c \\ 0, & \text{otherwise.} \end{cases} \quad (11)$$

This profile diverges as $|V_{\text{obs}}| \rightarrow V_c$, but the resulting singularity is smoothed by introducing a constant velocity dispersion for gas of $\sigma_{\text{gas}} = 10 \text{ km s}^{-1}$ throughout the disc, which mimics the effect of random $\text{H}\alpha$ motions. This assumption is supported by observations of the gas velocity dispersion seen in the nearby galaxies (Leroy et al. 2008). The smoothed normalized velocity profile is then given by

$$\psi(V_{\text{obs}}, V_c) = \frac{\sigma^{-1}}{\sqrt{2\pi}} \int dV \exp \left[\frac{(V_{\text{obs}} - V_c)^2}{-2\sigma^2} \right] \tilde{\psi}(V_{\text{obs}}, V_c). \quad (12)$$

From the edge-on line profile $\psi(V_{\text{obs}}, V_c)$ of a single ring and the surface density of atomic hydrogen, $\Sigma_{\text{H}\alpha}$, which has been calculated as described in Section 3.1, we can construct the edge-on profile of the $\text{H}\alpha$ emission line for the entire $\text{H}\alpha$ disc, by using the following equation,

$$\Psi_{\text{H}\alpha}(V_{\text{obs}}) = \frac{2\pi}{M_{\text{H}\alpha}} \int_0^\infty dr r \Sigma_{\text{H}\alpha}(r) \psi(V_{\text{obs}}, V_c(r)). \quad (13)$$

An example of the resulting $\text{H}\alpha$ emission lines is shown in Fig. 4, where we can see the signature double-horned profile. We include the effect of inclinations by using the inclination provided by STINGRAY for every galaxy in the light-cone.

To construct the $\text{H}\alpha$ emission lines, we assume a constant $\text{H}\alpha$ velocity dispersion. Observations have found the latter to be remarkably constant, with values typically ranging from 8 to 12 km s^{-1} (Leroy et al. 2008), and approximately independent of galaxy properties. This has been suggested to be caused by thermal motions setting the $\text{H}\alpha$ velocity dispersion, and the $\text{H}\alpha$ abundance being largely dominated by the warm, neutral interstellar medium. Hence, we decide to keep this value constant, but note that increasing (decreasing) σ_{gas} has an effect of slightly increasing (decreasing) the number of low W_{50} galaxies, $\lesssim 40 \text{ km s}^{-1}$ in Fig. 9.

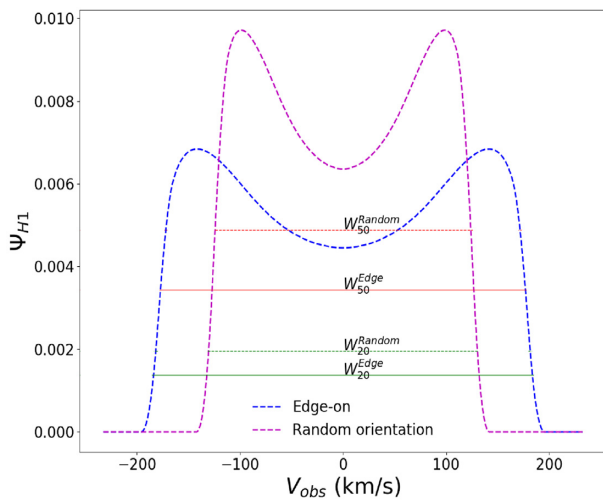


Figure 4. Normalized H I emission-line profile for the same example galaxy of Figs 2 and 3, with edge-on and intrinsic inclination of the randomly selected galaxy (in this case, $\cos(\theta) \sim 60^\circ$), as labelled. The two top and the two bottom horizontal lines mark the W_{50} and W_{20} of the two orientations respectively. W_{50} and W_{20} are maximal at edge-on orientations.

3.4 Flux calculation

The lines described in Section 3.3 are normalized, and so need to multiply by the integrated flux of the H I line to approximate an observed H I emission line, which we do by using the relation of

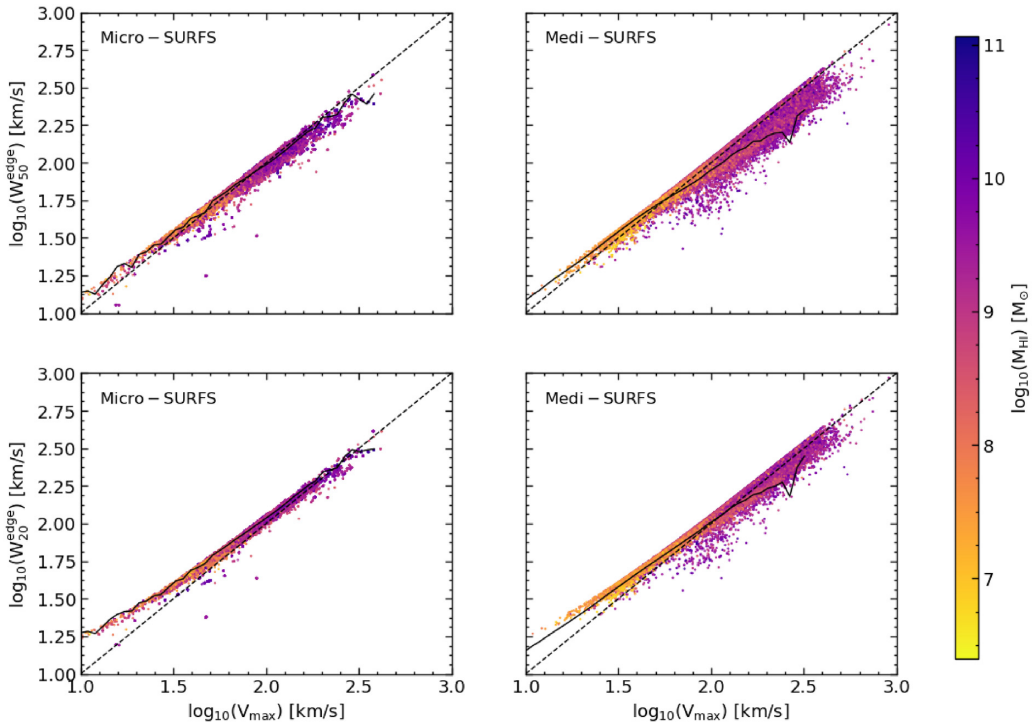


Figure 5. Comparison of the intrinsic maximum circular velocities of SHARK galaxies with that derived from our mock observations of the galaxies, using the width at 50 per cent (top row) and 20 per cent (bottom row) of the peak flux of the H I emission lines of the simulated galaxies. The dashed and solid lines represent the 1:1 line and median of the values, respectively, with each scatter point being an individual galaxy in the simulation, and coloured by their H I mass, as shown in the colour bar at the right of the figure. A slight tendency to deviate up from the 1:1 relation is seen at $V_{\max} \lesssim 30 \text{ km s}^{-1}$, which is caused by the fact that the H I velocity dispersion and rotational velocity become comparable at such low velocities. As W_{20} is measured at a lower level than W_{50} it gets affected more by the dispersion than W_{50} .

Catinella et al. (2010b),

$$\frac{M_{\text{HI}}}{M_{\odot}} = \frac{2.356 \times 10^5}{1+z} \left[\frac{d_L(z)}{\text{Mpc}} \right]^2 \left(\frac{\int S d\Omega}{\text{Jy km s}^{-1}} \right); \quad (14)$$

here M_{HI} is the H I mass, $d_L(z)$ is the luminosity distance of the galaxy at redshift z , and $\int S d\Omega$ is the integrated flux. The luminosity distance and redshift information were obtained from the ALFALFA light-cone produced in the Section 2.1 and the H I mass is directly output by SHARK.

3.5 How well does the H I velocity width trace V_{\max} ?

Fig. 5 compares V_{\max} and the 50th percentile, W_{50} , and 20th percentile, W_{20} , widths of the H I emission lines in the case of edge-on orientations, for all galaxies in the ALFALFA light-cone (see Section 3.2 for a description of V_{\max}); W_{50} and W_{20} are widely used in the observations to estimate rotational velocities of galaxies.

Fig. 5 shows that there is good agreement between the true maximum circular velocities and the simulated H I W_{50} and W_{20} at the higher velocity regime, $V_{\max} \gtrsim 100 \text{ km s}^{-1}$, but there are systematic deviations at lower velocities, $V_{\max} \lesssim 35 \text{ km s}^{-1}$. These deviations can be understood as the effect of non-circular motions modelled via the inclusion of the random H I velocity component to the H I emission lines. As stated in Section 3.3, we incorporate a velocity dispersion of 10 km s^{-1} throughout the H I disc. When we reach the low velocity range ($\lesssim 35 \text{ km s}^{-1}$), this velocity dispersion is comparable to these circular velocity of the disc and skews the H I linewidths. We should also note that the direction

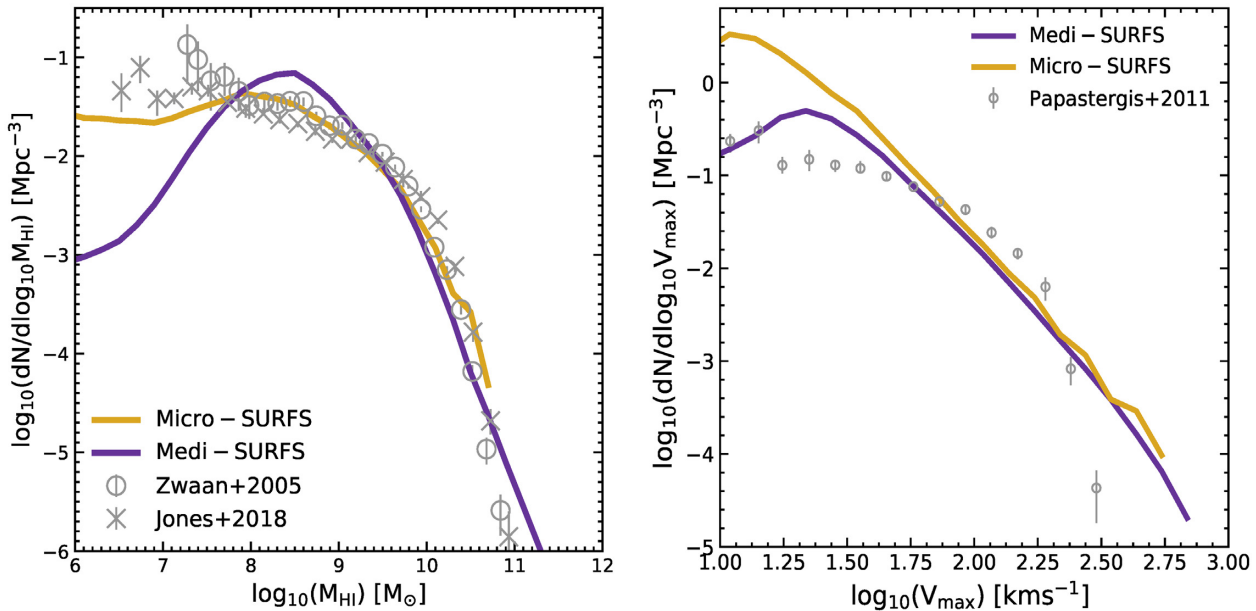


Figure 6. The H α mass function (left-hand panel) and H α VF (right-hand panel) of all the SHARK galaxies at $z = 0$, produced using the medi-SURFS and micro-SURFS, as labelled in each panel. We also show as symbols the observational estimates from Zwaan et al. (2005) and Jones et al. (2018) in the case of the H α mass function, and from Papastergis et al. (2011) for the H α VF. There is good agreement between the SHARK and the observations of the H α mass function, while there is a clear tension with the observations of the H α VF at $V_{\text{mas}} \lesssim 100 \text{ km s}^{-1}$.

of this skewness is the opposite to what Brooks et al. (2017) found in their cosmological hydrodynamical zoom simulations of dwarf to MW galaxies. In spite of this effect, however, we can recover the observed H α velocity and mass distributions (Section 4.2).

3.6 H α line profiles: idealized models versus hydrodynamical simulations

As discussed in Section 3, we assume profiles for our DM, gas, and stellar components when modelling the H α emission lines of all SHARK galaxies. In addition, we also assume axisymmetry that leads to perfect double-horned H α emission line profiles for our SHARK galaxies. Observations show that asymmetries in the H α emission-line profiles are common (Catinella et al. 2010a) and hence we would like to test how much our assumptions affect our ability to predict a distribution of W_{50} and W_{20} .

With this aim, we use a suite of 13 dwarf and 2 MW-sized galaxies from the APOSTLE cosmological hydrodynamical simulations suite (Sawala et al. 2016) as a test-bed, and use the MARTINI (Oman et al. 2019) software to produce H α emission lines for all these galaxies (see Appendix A for details). We find that our idealized model reproduces very well the W_{20} measurements of the APOSTLE simulations. However, the W_{50} measurements show more discrepancies driven by the asymmetry of the H α emission lines in the APOSTLE simulations. These deviations are typically within ≈ 25 per cent in the case of dwarf galaxies $V_{\text{max}} \lesssim 100 \text{ km s}^{-1}$, while being larger for the two MW galaxies. Because we are interested primarily in the dwarf regime, we conclude that our idealized H α emission-line model produces a good enough representation of dwarf galaxies even in hydrodynamical simulations.

4 REPRODUCING THE H α MASSES AND VELOCITIES OF OBSERVED GALAXIES IN A Λ CDM FRAMEWORK

We compare SHARK predictions with H α observations to highlight the conclusions one could draw in such case. We then go onto comparing our simulated ALFALFA survey with the real one and discuss our findings.

4.1 A raw comparison between SHARK and the observed H α masses and velocities of galaxies

The traditional way in which simulations are compared to observations is by taking the predicted galaxy population in the simulated box and comparing directly with derived properties of galaxies in observational surveys. The drawback of such an approach is that there may be important selection biases that are not taken into consideration. This could lead us to conclude that the simulation fails to reproduce an observable when in fact it reflects a mismatch in the different selections and biases that are present in simulation and observational data. This hampers interpretation of the shortcomings of simulations and our understanding of galaxy formation.

In this context, we examine the raw SHARK predictions with the derived ALFALFA H α mass and VFs, which should illustrate the importance of accounting for selection effects. We do the comparison using both the micro-SURFS and medi-SURFS (see Section 2 for details) simulations, and perform a raw comparison with ALFALFA. This assumes that observations are able to sample an unbiased portion of the galaxy population across the probed dynamic range and hence, a reliable volume correction can be applied to take the observed distributions to convert them into functions.

In the left-hand panel of Fig. 6, we compare the H α mass function at $z = 0$ that we derive from SHARK, running over the two simulation boxes described in Introduction, with the observed H α mass function

at $z = 0$ from Jones et al. (2018) and Zwaan et al. (2005), and find overall agreement between the predictions and observations. Micro-SURFS agrees better with the observations across the whole dynamic range of masses observed, while medi-SURFS agrees well with the observations at $M_{\text{HI}} \gtrsim 10^9 M_{\odot}$, while deviating at lower H I masses. This difference is simply a resolution effect, in which the haloes that host central galaxies with $M_{\text{HI}} \lesssim 10^9 M_{\odot}$ are not well resolved in medi-SURFS, but they are in micro-SURFS. The median halo mass for central galaxies of $M_{\text{HI}} \lesssim 10^9 M_{\odot}$ is $M_{\text{Halo}} \lesssim 10^{11.4} M_{\odot}$ in the medi-SURFS, which would comprise of ~ 1100 particles in them. On the other hand, micro-SURFS has a similar median halo mass for central galaxies below $M_{\text{HI}} \lesssim 10^9 M_{\odot}$, but because of better mass resolution such halo masses are made of ≈ 6000 particles, and so is able to better resolve the haloes over the dwarf galaxy mass range. The agreement between SHARK and observations is not surprising because Lagos et al. (2018) used the H I mass function as a guide to find a suitable set of values for the free parameters in SHARK.

In the right-hand panel of Fig. 6, we show the comparison between the 40 per cent ALFALFA data release global H I VF at $z = 0$ as calculated by Papastergis et al. (2011) and the ‘raw’ H I VFs of the circular velocities of the galaxies at $z = 0$ in SHARK, again for our two simulations, medi-SURFS and micro-SURFS. This allows us to determine whether or not SHARK overpredicts the number of low dynamical mass systems as reported in Zavala et al. (2009), Schneider et al. (2017), Papastergis et al. (2011), and Obreschkow et al. (2013). We find that more galaxies are predicted than are observed by more than an order of magnitude at circular velocities $< 100 \text{ km s}^{-1}$. The peak of the VF for micro-SURFS is shifted towards a lower velocity ($\sim 20 \text{ km s}^{-1}$) due to its higher mass resolution, which enables us to better sample the low dynamical mass galaxies at the cost of producing a smaller number of massive galaxies. The latter is due to the smaller volume. This problem is remedied by including medi-SURFS, which allows us to access much larger cosmological volumes and hence higher dynamical masses. The downside is that its resolution is coarser and hence does not go down to the low halo masses that we have access to with micro-SURFS. The two simulations in combination allow us to fully sample the velocity and H I mass range of interest, $\approx 20\text{--}800 \text{ km s}^{-1}$. We confirm previous results that have reported an overabundance of low-dynamical mass galaxies in ΛCDM compared to observations, even after accounting for the complexity of how galaxies populate haloes through the modelling of SHARK.

Because we are investigating the masses and velocities of galaxies, it is natural to extend the comparison to the Tully–Fisher relation (Tully & Fisher 1977), which is an empirical relation between the optical luminosity and the W_{50} of H I emission lines. The Tully–Fisher relation has been used to place tight constraints on galaxy formation models and is used as a test for the robustness of those models (e.g. Fontanot, Hirschmann & De Lucia 2017). McGaugh (2011) extended the classic Tully–Fisher relation to the baryonic Tully–Fisher relation (BTFR), which relates the total baryonic mass of galaxies (gas plus stars) with the observed rotational velocities. In Fig. 7, we compare the predicted BTFR of all disc-dominated (bulge-to-total ratio < 0.5) SHARK galaxies (open symbols) with the observed BTFR of McGaugh (2011). Here, we only show the micro-SURFS because the medi-SURFS results are similar, albeit lacking the lowest V_{circ} galaxies. We find that the simulated galaxies tend to be $\approx 0.2\text{--}0.3$ dex more H I massive at fixed circular velocity compared to observations. If instead we use the edge-on H I W_{50} of galaxies that are present in our mock survey, we find that they follow the BTFR more closely. This result further strengthens our confidence

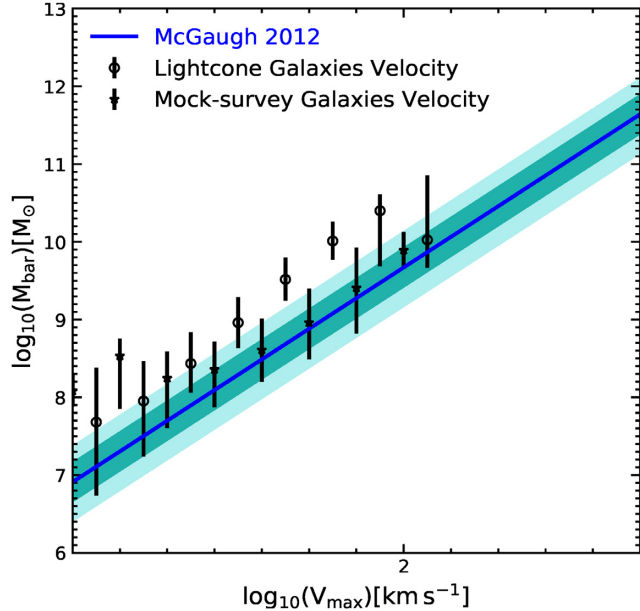


Figure 7. The BTFR of all the galaxies in the light-cone compared to those that we flag as ‘ALFALFA-selected’ in the light-cone. We also show the best fit to the observed relation from McGaugh (2011). We show the results from the micro-SURFS box only as there was little difference in the values from medi-SURFS. The figure shows that the entire galaxy population follows a Tully–Fisher relation in tension with the observations, while the more fair comparison with the ‘ALFALFA-selected’ simulated galaxies shows much better agreement, showing that SHARK galaxies reproduce the Tully–Fisher relation very well.

in that the H I W_{50} measurements done in this study are a closer representation of the observed H I W_{50} than raw circular velocity.

4.2 A mock-to-real comparison between SHARK and ALFALFA

The ALFALFA survey is a ‘blind’ H I survey that has mapped nearly 7000 deg^2 area in the velocity range $-2000 < cz < 18000 \text{ km s}^{-1}$, where c is the speed of light and z is the redshift. The survey has identified ~ 31500 extragalactic H I line sources (Haynes et al. 2018). The detection limit of the survey as described by Papastergis et al. (2011) is a function of the integrated H I line flux, $S_{\text{int, lim}}$, and velocity width $S_{\text{int, lim}}/\text{Jy km s}^{-1} = 0.06 (W_{50}^{0.51}/\text{km s}^{-1})$.

For our analysis, we apply the same selection of Papastergis et al. (2011) to our light-cones (see Section 2.1 for details) to select ALFALFA-like galaxies; this results in our mock ‘ALFALFA’ survey. We remind the reader that our light-cone has the same survey area and redshift coverage as ALFALFA. We also apply beam confusion to the light-cone prior to applying the selection criterion above.

We construct the H I mass distribution from the released catalogue of Haynes et al. (2018), and present this as number per unit deg^2 . The resulting observed distribution is shown in Fig. 8 as symbols. We perform the same measurement in our mock ALFALFA survey (one for each SURFS simulation being used here), which we also show in Fig. 8. We find that there is very good agreement between the simulated and observed H I mass distributions, which is particularly striking for the light-cone based on micro-SURFS. This is not surprising, because Fig. 8 shows that the predicted H I mass function agrees well with the measurements of Jones et al. (2018). There is a

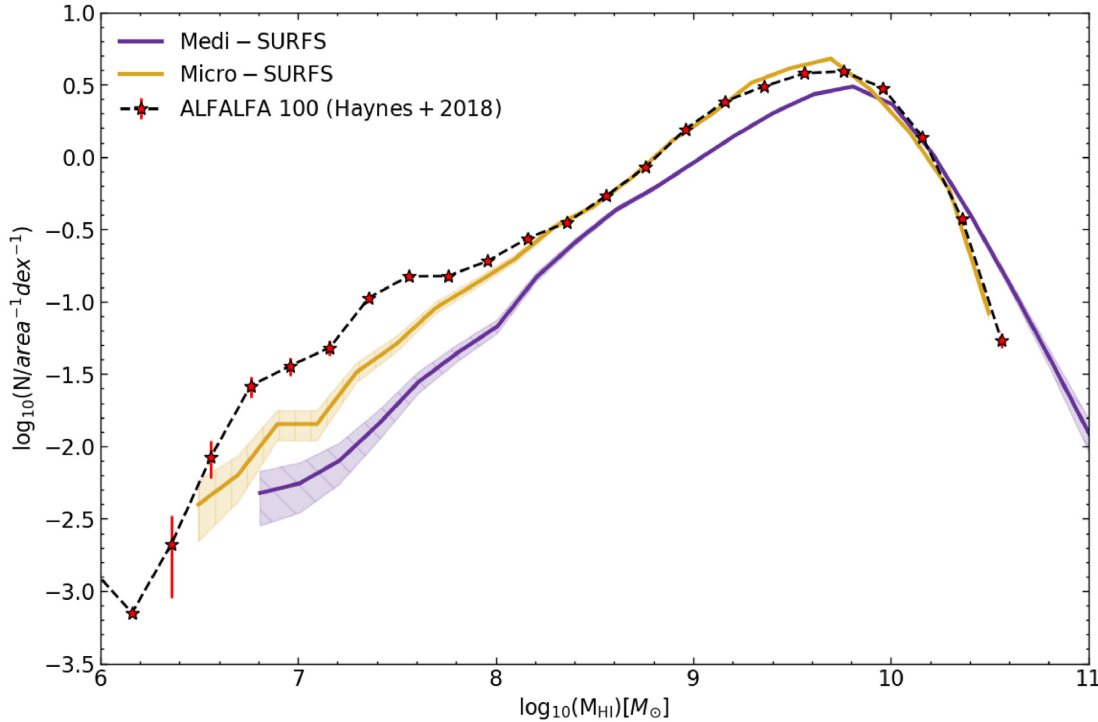


Figure 8. Comparison of the $\text{H}\alpha$ mass distribution as obtained from our mock ALFALFA survey with the observations of Haynes et al. (2018). The purple and yellow solid lines represent the results of the light-cones constructed with SHARK, using the medi-SURFS and micro-SURFS N -body simulations, respectively. The shaded region is representative of the poisson noise in the data. Our mock survey’s $\text{H}\alpha$ mass distribution, in both resolution boxes, is in reasonable agreement with the observations.

slight tension between $\text{H}\alpha$ masses of 10^7 and 10^8 M_\odot , where SHARK predicts a slightly lower number of galaxies. Lagos et al. (2018) showed that the abundance of galaxies below the break of the $\text{H}\alpha$ mass function was very sensitive to the adopted parameters in the photo-ionization model. Lower velocity thresholds, below which haloes are not allowed to cool gas to mimic the impact of a ultraviolet background, has the effect of producing a higher abundance of low $\text{H}\alpha$ mass galaxies (see their appendix A).

In this work, we do not attempt to calibrate SHARK to reproduce the low-mass end of the $\text{H}\alpha$ mass function but simply to show how our default model performs compared to $\text{H}\alpha$ observations, and to put constraints on the magnitude of the discrepancy (if any) between the predictions and the observations of $\text{H}\alpha$ masses and velocity widths.

We now turn our attention to the $\text{H}\alpha W_{50}$ distribution. We take the $\text{H}\alpha W_{50}$ measurements from Haynes et al. (2018, which are as observed, and hence there is no attempt to correct by inclination effects), and construct the $\text{H}\alpha W_{50}$ distribution (shown as symbols in Fig. 9). We also take our modelled $\text{H}\alpha W_{50}$ (assuming the STINGRAY inclinations for our simulated galaxies) and construct the $\text{H}\alpha W_{50}$ distribution for those that pass the ALFALFA selection criterion for our two light-cones created running SHARK on the medi- and micro-SURFS (lines in Fig. 9, as labelled). We find that the model and the observations agree remarkably well. We remind the reader that the observationally derived $\text{H}\alpha$ VF and the V_{\max} function of SHARK displayed differences of factor $\gtrsim 20$ at velocities $\lesssim 30 \text{ km s}^{-1}$ (see Fig. 6), while in Fig. 9, differences are $\lesssim 50$ per cent. In other words, the ‘missing dwarf galaxy problem’ is not evident. Using the medi- and micro-SURFS allow us to probe the entire range of the observations with the micro-SURFS simulation probing the lower velocity end $\lesssim 30 \text{ km s}^{-1}$, while the medi-SURFS allows us to improve significantly the statistics at the high $\text{H}\alpha W_{50}$ end

$\gtrsim 100 \text{ km s}^{-1}$. With SHARK applied to these two simulations, we are able to reproduce the observed $\text{H}\alpha W_{50}$ distribution. The large differences seen between Figs 6 and 9 suggests that there are important selection biases which cannot be easily corrected in the process of taking the observed $\text{H}\alpha W_{50}$ distribution and inferring from there an $\text{H}\alpha W_{50}$ function, which prevent us from making a one-to-one comparison between the predicted V_{\max} function from DMO simulations and observations. This highlights the fact that building light-cones to reproduce observational surveys is essential to tackle this problem, and, in their absence, erroneous conclusions could be drawn.

We have so far shown that SHARK produces galaxies with the correct $\text{H}\alpha$ mass and W_{50} distributions, but that does not necessarily mean that galaxies of a given $\text{H}\alpha$ mass have the right $\text{H}\alpha W_{50}$. To test this, Fig. 10 shows 2D histograms of galaxies in the $\text{H}\alpha$ mass- W_{50} plane. The left-hand panel shows all the galaxies in the simulation at $z = 0$, whose numbers are scaled accordingly to match the ALFALFA volume, whereas the right-hand panel shows the galaxies which pass the ALFALFA selection criterion applied to our light-cones. We also show the same 2D histograms of galaxies for the real ALFALFA survey in the bottom, right panel of Fig. 10. Going from left- to right-hand panels of Fig. 10 show that the majority of galaxies that were originally present in simulation box do not satisfy the ALFALFA selection. Large differences are seen between the 2D distributions of the galaxies in the $z = 0$ simulated boxes and the mock ALFALFA light-cones. Most of the galaxies in both micro- and medi-SURFS with masses $M_{\text{H}\alpha} \lesssim 10^9 \text{ M}_\odot$ are selected out, producing a narrower relation between $\text{H}\alpha$ mass and W_{50} than the one followed by the underlying population of simulated galaxies. Our simulated ALFALFA light-cone reproduces well the observed $\text{H}\alpha$ mass and W_{50} relation of ALFALFA. However, there is

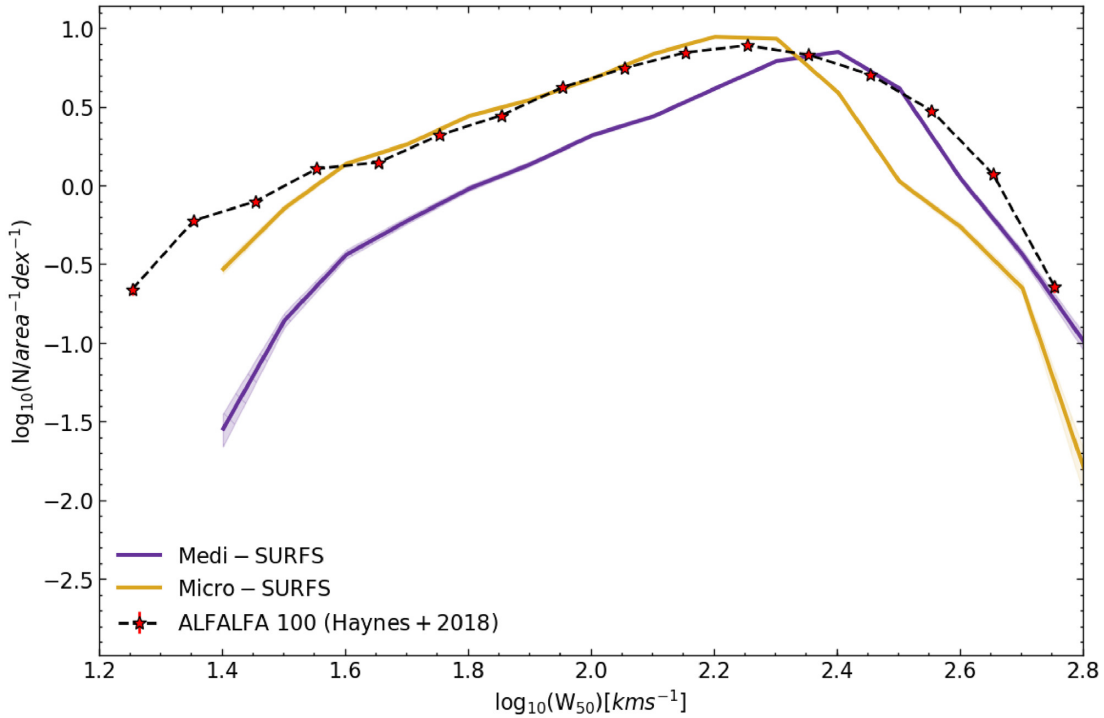


Figure 9. The H I velocity distribution obtained by our mock ALFALFA survey, with the purple and yellow solid lines representing the SHARK model run over the medi- and micro-SURFS simulations, respectively, with the shaded regions representing the poisson noise. Because micro-SURFS has a higher resolution than medi-SURFS, it traces the lower velocity end better, while the medi-SURFS is able to track down the galaxies at higher velocity end. By combining the results from these two boxes and applying the selection function of ALFALFA, we are able to obtain a VF that is in agreement with the observations.

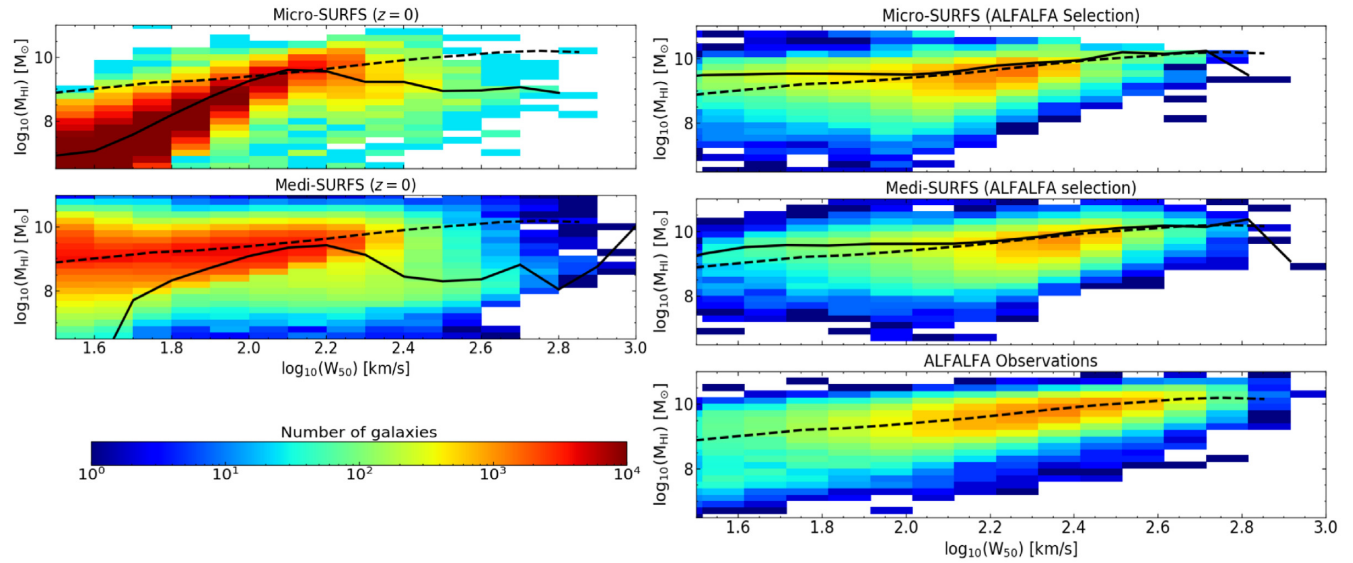


Figure 10. 2D histograms showing the number of galaxies in the plane of H I mass and W_{50} for the SHARK galaxies obtained by running the model in the medi- and micro-SURFS, as labelled. The left-hand panels show *all* the galaxies in the simulation at $z = 0$, which we scale accordingly to match the volume of ALFALFA, whereas the right-hand panels show only the galaxies that are comply with the ALFALFA selection in our mock survey. The bottom, right-hand panel shows the actual observed H I mass– W_{50} relation of the ALFALFA survey as released in Haynes et al. (2018). The colour bar indicates the number of galaxies present in each bin. Solid lines show the running median for that respective panel, whereas the dashed line is the running median for the ALFALFA observations. Most galaxies in the model are below the ALFALFA selection criterion which is why the relations look so different between the left- and right-hand panels. Anyhow, the similarity to the actual observations gives us the confidence that we are detecting similar galaxies in our mock survey.

some tension in the medians as SHARK tends to produce 0.1–0.4 dex too much H I mass at $\log_{10}(W_{50}/\text{km s}^{-1}) \lesssim 2.1$. This difference is

also seen in Fig. 8, as the number of galaxies in the simulations is less than the observed one in the regime of $M_{\text{HI}} \lesssim 10^8 M_{\odot}$.

In Figs 11 and 12, we show the biases the selection criterion of ALFALFA introduces in the galaxy population; in other words, how do ALFALFA-like galaxy properties compare to the underlying galaxy population? In both figures, the red and the blue colours represent all galaxies in the light-cone (prior to any selection) and the ALFALFA mock-survey galaxies (after applying the ALFALFA selection), respectively.

Fig. 11 and the right-hand panel of Fig. 12 show the half-gas mass disc radius, $\text{H}\alpha$ -to-stellar mass ratio and SFR as a function of the galaxy stellar mass, for all galaxies in SHARK and selected by the ALFALFA criteria (i.e. those that make up the distributions of Figs 8 and 9). The left-hand panel of Fig. 12 compares the $\text{H}\alpha$ content of the galaxies with its DM halo circular velocity, for the sub-sample of central galaxies in both SHARK and in those selected as ALFALFA-like. When comparing the gas radii (see left-hand panel in Fig. 11), we see that the median of the ALFALFA mock survey galaxies is always higher than the overall median of galaxies in SHARK (i.e. the underlying galaxy population), with our simulated ALFALFA galaxies having a half-gas mass radius of the disc $\approx 0.5\text{--}0.7$ dex larger than SHARK galaxies of the same stellar mass at $M_* \lesssim 10^{10.3} M_\odot$. A drop in the half-gas mass radii of galaxies at stellar masses higher than $10^{10.3} M_\odot$ is seen for the overall median of the SHARK galaxies (red). The latter is due to this mass range being dominated by passive elliptical galaxies which tend to be gas poor. This drop is not seen in the median of the ALFALFA mock survey galaxies (blue), thus showing that ALFALFA preferentially picks out gas-rich galaxies, avoiding early-type galaxies that are affected by AGN feedback. This preference is clear when we compare the $\frac{M_{\text{HI}}}{M_*}$ ratio for both observed and all galaxies in the SHARK (see right-hand panel in Fig. 11), with the mock ALFALFA survey galaxies, which continue to be systematically gas richer than the overall median, even at the dwarf galaxy regime.

We also see a strong preference for gas-rich galaxies when we compare the maximum circular velocity of central galaxies with their $\text{H}\alpha$ content (see left-hand panel in Fig. 12), with the mock observed galaxies median (blue) staying in the range of $10^8 \lesssim M_{\text{HI}} \lesssim 10^{10} M_\odot$, even when the overall median (red) is orders of magnitude below ($M_{\text{HI}} \sim 10^6\text{--}10^8 M_\odot$). Even though both ALFALFA and our mock ALFALFA survey detect galaxies with $\text{H}\alpha$ content as low as $10^6 M_\odot$, the number of those detections are fairly low ($\sim 20\text{--}30$ galaxies), making the higher $\text{H}\alpha$ mass galaxies more dominant and skewing the median towards those values even at the low circular velocity end.

When analysing the overall central galaxy population, there is a clear peak in the $M_{\text{HI}} - V_{\text{max}}$ relation, which is related to the peak of the baryon collapse efficiency in galaxies (e.g. Eckert et al. 2017). Baugh et al. (2019) using the GALFORM semi-analytic model of galaxy formation (Cole et al. 2000; Lacey et al. 2016; Lagos et al. 2014) also found a sharp break in the $\text{H}\alpha$ mass–halo mass relation at $\gtrsim 10^{11.5} M_\odot$. This is the approximate halo mass scale at which AGN feedback starts to suppress gas cooling in both models, leading to the decline in $\text{H}\alpha$ mass. The width and prominence of the peak is therefore expected to be very sensitive to the AGN feedback model and hence a useful relation to constrain from observations.

When comparing the SFR with the stellar mass (see right-hand panel in Fig. 12), we see only a small tendency for the ALFALFA mock survey galaxies to have slightly higher SFRs than the underlying galaxy population, again across the whole stellar mass range studied here. The most probable reason for this effect is that in SHARK the SFR is calculated from the H_2 content of the galaxies, which in turn depends on the total gas mass and

radius. Because gas masses are larger in the ALFALFA mock survey galaxies compared to the underlying population, that tends to drive a smaller H_2/HI ratio, which is why the SFRs in Fig. 12 are close to the median of SHARK despite the higher $\text{H}\alpha$ abundance in Fig. 11. The main sequence of SF of the entire sample of light-cone galaxies shows a clear break at $\sim 10^{10} M_\odot$, driven by the mass above which AGN feedback starts to be important (typically overcoming the gas cooling luminosity). This break is not seen in the ALFALFA mock survey galaxies, showing the strong bias against gas poor, low star-forming galaxies.

These biases are to be expected because ALFALFA is a blind survey and is limited by the integrated $\text{H}\alpha$ flux and velocity width, which in turn depends on the $\text{H}\alpha$ mass content of galaxies. What is unexpected is that these biases are important even at the dwarf galaxy regime, where most galaxies are star-forming and gas-rich; our ALFALFA mock survey galaxies are more gas-rich and more star-forming. This also raises concerns regarding how best to correct for the galaxies that are not detected by ALFALFA, and how to account for the fact that the observed population is not representative even at the dwarf galaxy regime. Thus, we can see that selection bias plays a very important role in our understanding of the intrinsic galaxy properties and are crucial even at dwarf galaxy scales.

4.3 Implications for ΛCDM and comparisons with previous studies

Brooks et al. (2017) used a suite of 33 cosmological zoom hydrodynamical simulations, covering a wide dynamic range from dwarfs to MW-like galaxies, and suggested that the dearth of observed galaxies with low circular velocities was caused by the $\text{H}\alpha$ linewidth (used as the dynamical mass tracer) not tracing the full potential well in dwarf galaxies. The reason for this was because in their simulated dwarf galaxies, the bulk of $\text{H}\alpha$ is in the rising part of the rotation curve, which means that the integrated $\text{H}\alpha$ linewidth does not reflect the maximum circular velocity of the galaxy. This results in a relation between the effective circular velocity of $\text{H}\alpha$ ($V_{\text{H}\alpha} = W_{50}/2$ for a galaxy observed edge-on) and the maximum circular velocity which significantly deviates from the 1:1 relation at the dwarf galaxy regime, in a way that in the latter $V_{\text{H}\alpha}$ is much smaller than V_{max} . By applying the relation $V_{\text{H}\alpha} - V_{\text{max}}$ obtained from their zoom simulations to the DM haloes of a large cosmological volume, DMO simulation, they were able to reproduce the observed galaxy VF. This therefore offers an attractive solution to the tension seen in Fig. 6, which is also supported by the fact that there have been reports from observations in some nearby dwarfs that the bulk of $\text{H}\alpha$ is indeed in the rising part of the rotation curve e.g. Catinella, Giovanelli & Haynes (2006), Swaters et al. (2009), and Oman et al. (2019).

Macciò et al. (2016) arrived at a similar conclusion, but using mock-observed galaxies from the NIHAO simulations suite (a suite of 100 cosmological hydrodynamical simulations zooms, again covering a wide dynamic range from dwarfs to MW-like galaxies Wang et al. 2015). They obtained similar deviations of the $V_{\text{H}\alpha} - V_{\text{max}}$ relation from the 1:1 line at the dwarf galaxy regime as Brooks et al. Two reasons were given by Macciò et al. (2016) to explain this, one was again the fact that $\text{H}\alpha$ is not extended enough to reach the flat part of the rotation curve, and the second was that the non-circular motions of the gas seem to become significant at the dwarf galaxy regime (also seen in other cosmological zoom simulations; e.g. Oman et al. 2019). Despite this impressive progress, an important limitation remains. Both studies, Macciò et al. (2016) and Brooks et al. (2017), assume their suite

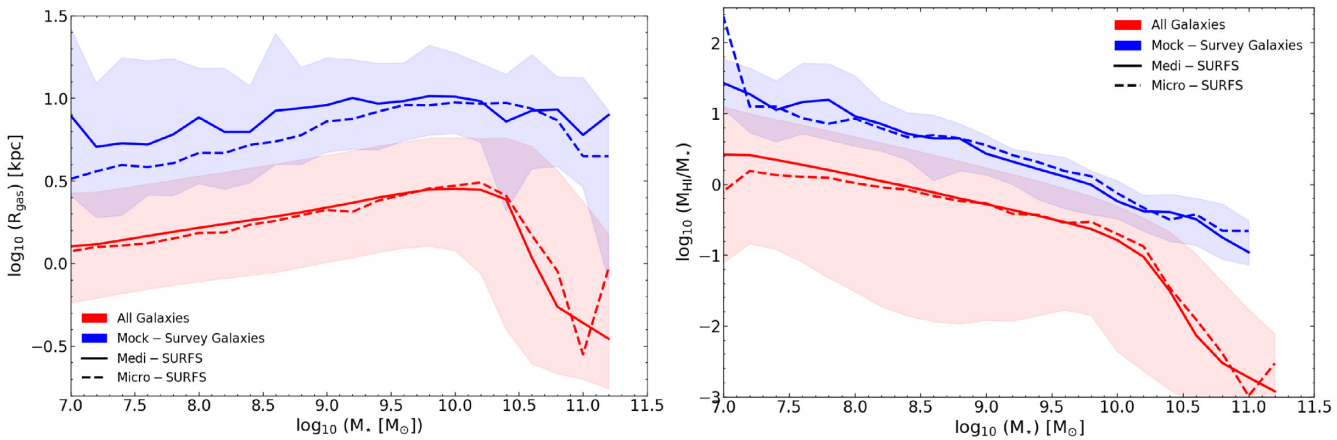


Figure 11. Half-gas mass disc radius (left-hand panel) and H_I-to-stellar mass ratio (right-hand panel) as a function of stellar mass of the galaxies at $z = 0$ in SHARK. The lines and colours represent our two simulations medi- and micro-SURFS, as labelled. Shaded regions show the 16th–84th percentiles. For clarity, the latter are shown only for the medi-SURFS. A clear selection effect is seen as galaxies with larger gas discs and higher gas-to-star ratio are preferentially selected by ALFALFA.

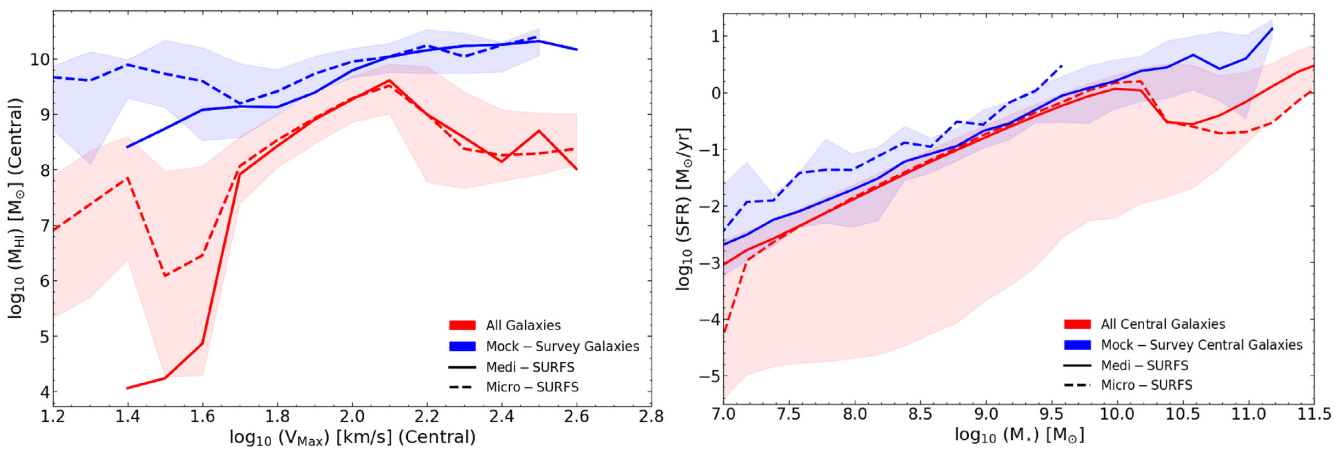


Figure 12. Left: H_I content of galaxies as a function of the maximum circular velocity of the galaxy (which is used as a proxy for dynamical mass). Due to the limited resolution of medi-SURFS, we only show the latter down to $\log_{10}(V_{\max}/\text{km s}^{-1}) = 1.4$. Resolution is the likely driver of the difference seen between medi- and micro-SURFS below $\log_{10}(V_{\max}/\text{km s}^{-1}) \approx 1.7$. Here, we show the 16th–84th percentiles for micro-SURFS as it goes down to lower circular velocities. Right: as Fig. 11, but for the SFR as a function of the stellar mass. In both panels, a clear bias is seen as the ALFALFA mock survey is preferentially selecting galaxies with higher H_I content, albeit a smaller bias is seen for the SFR.

of simulated galaxies to be representative of all the galaxies of the same V_{\max} . The main question is then whether 33 or 100 galaxies is sufficient to make a statement about the main drivers of the tension seen in Fig. 6.

To address this question, we turn to our ALFALFA light-cones and quantify the fraction of galaxies at two maximum circular velocities, $V_{\max} = 100$ and 30 km s^{-1} that would be selected by ALFALFA (given their selection criteria) in a fixed cosmological volume. These V_{\max} values are chosen because the deviations of the $V_{\mathrm{H}\mathrm{I}} - V_{\max}$ relation from the 1:1 line in Macciò et al. (2016) and Brooks et al. (2017) appear at $V_{\max} \lesssim 100 \text{ km s}^{-1}$. In SHARK, we find that ≈ 22 per cent of the galaxies with $V_{\max} = 100 \text{ km s}^{-1}$ would be detectable by ALFALFA, while that number reduces to ≈ 1.4 per cent for galaxies with $V_{\max} = 30 \text{ km s}^{-1}$. In the context of the simulated samples of Macciò et al. (2016) and Brooks et al. (2017), a few galaxies with $V_{\max} = 100 \text{ km s}^{-1}$ and < 1 (or ~ 0.462) galaxy with $V_{\max} = 30 \text{ km s}^{-1}$ would be detectable by ALFALFA.

In addition, the small fraction of dwarf galaxies that would be detectable by ALFALFA is far from representative of the galaxies that have on average the same stellar or halo mass. This strongly argues for the need of large statistics to assess the tension between Λ CDM and the observed galaxy VF of Fig. 6.

Our work therefore differs from previous ones in two fundamental ways. The first is that we use a statistically significant population of galaxies; with each simulated box having ~ 1.3 million galaxies, each of which have their own SF, gas accretion, and assembly histories, and so we are capable of simulating the entire ALFALFA survey volume. The second is that is that we obtain a $V_{\mathrm{H}\mathrm{I}} - V_{\max}$ relation that is very close to the 1:1 line even at the dwarf galaxy regime. Hence, we are able to reproduce the observed H_I W_{50} distribution *without* the need to invoke significant deviations in the $V_{\mathrm{H}\mathrm{I}} - V_{\max}$ relation. That is not to say these deviations do not exist but simply that *observations can be reproduced without them*. The fact that our model does not obtain the deviations discussed above is

likely due to the simplistic physics that is inherent to semi-analytic models, which are much better captured with hydrodynamical simulations, and therefore likely reflects a limitation of our model. In Appendix A, we applied our idealized model to galaxies in the APOSTLE hydrodynamical simulation suite, and found that in dwarf galaxies our method overestimates W_{50} by ≈ 20 – 30 per cent. If we were to correct out W_{50} distribution of Fig. 9 by these differences, our predicted number of dwarf galaxies would slightly decrease, making the number of dwarfs *smaller* than the observed one – indicating that the observed abundance of low W_{50} galaxies is very sensitive to baryon physics.

Our work suggests that the main effect in the apparent discrepancies between the predicted V_{\max} function from DMO simulations and the recovered one from observations are selection effects, which are complex because of how non-linearly galaxy properties correlate with their halo properties. Hence, the $H\alpha$ velocity distribution is not a cosmological test, but more appropriately a baryon physics test. This also strongly suggests that for a complete and unbiased understanding of $H\alpha$ galaxy surveys, it is necessary to mock observe our simulated galaxy population and compare with observations in a like-to-like fashion.

5 CONCLUSIONS

The abundance of galaxies of different maximum circular velocities (the VF) is a fundamental prediction of our concurrent cosmological paradigm and hence, of uttermost important to test against observations. In this work, we have used the SHARK semi-analytic galaxy formation model to simulate the ALFALFA $H\alpha$ survey, the largest blind $H\alpha$ survey to date, to investigate the well-known discrepancy between the observed and predicted galaxy $H\alpha$ VF. Our goal was to determine whether this tension is a true failure of Λ CDM, or simply a reflection of the complexity of baryon physics.

We have presented how we model $H\alpha$ emission lines in SHARK taking into account halo, gas, and stellar radial profiles of galaxies, and tested our idealized approach against more complex models derived from the cosmological hydrodynamical APOSTLE simulations by comparing our derived $H\alpha$ linewidths with theirs and find good agreement. We used this new modelling to build a mock ALFALFA survey, and in the process, we combined simulation boxes spanning a range of mass resolutions and cosmological volumes, to ensure a good coverage over the full dynamical range probed by the observations. By applying the ALFALFA selection function to our simulated galaxies, we were able to recover the observed $H\alpha$ velocity and mass distributions to within 30 per cent, which shows that a physically motivated model of galaxy formation in the Λ CDM paradigm is able to reproduce the observed $H\alpha$ velocity width distribution of galaxies. We highlight that these are true predictions of our SHARK model, as gas properties are a natural outcome of the model and were not included in fine tuning of the free parameters of the model.

Our key results can be summarized as follows –

(i) Survey selection plays a major role in explaining the discrepancy between predictions and observations of the $H\alpha$ VF. We see an overprediction of galaxies in the $H\alpha$ VF of more than an order of magnitude at the low velocity end only when we make an ‘out-of-the-box’ comparison of the predicted and observed galaxy populations, while a careful comparison accounting for the survey selection criteria reveals discrepancies of less than 50 per cent. On applying the ALFALFA selection criteria, we get the desired $H\alpha W_{50}$

distribution even at low circular velocities, alleviating the missing dwarf galaxy problem.

(ii) Our predicted galaxy population agrees well with the observed $H\alpha$ mass function. We compare the $H\alpha$ - W_{50} 2D distribution obtained from the 100 per cent data release of ALFALFA with our mock survey, and find agreement at an acceptable level. This strengthens our belief that the discrepancy between the predicted $H\alpha$ velocity distribution with the observed one is due to the selection biases inherent in the survey.

(iii) Previous simulations found that the effective $H\alpha$ velocity ($V_{H\alpha} = W_{50}/2$ for an edge-on galaxy) significantly underestimates V_{\max} , which has been invoked as a plausible explanation for the discrepancies described above in the VF. We find that our $H\alpha$ emission-line modelling produces a $V_{H\alpha} - V_{\max}$ relation that is very close to the 1:1 line even at the dwarf galaxy regime. Despite this, we are able to reproduce the $H\alpha W_{50}$ distributions; these deviations may still happen, but we argue that they are not necessary to reproduce the observed $H\alpha W_{50}$ distribution.

(iv) A clear selection bias is seen when the mock is compared with the total galaxies that are presented in SHARK, shown in Figs 11 and 12. The mock ALFALFA survey is biased towards galaxies with a higher $H\alpha$ gas content, larger $H\alpha$ sizes and slightly higher SFRs. We find that at fixed V_{\max} the mock ALFALFA galaxies are very strongly biased towards high $H\alpha$ masses, with a difference in the typical $H\alpha$ mass of up to two orders of magnitude at $V_{\max} \approx 30$ – 50 km s^{-1} . This selection bias, in turn, affects our understanding of the distribution of galaxies in our local Universe. Thus in order to fully understand galaxy evolution, a clear understanding of these biases is required.

(v) By comparing our simple model of $H\alpha$ emission lines with the more complex $H\alpha$ lines obtained in the cosmological hydrodynamical simulation APOSTLE, we find that W_{20} is less affected by the asymmetry that is seen in the $H\alpha$ emission lines than W_{50} , the more commonly used velocity estimator. Thus, robust observational measurements of W_{20} would be extremely useful to constrain the simulations and uncover any tension with the simulations.

Our study suggests that the primary reason for the discrepancy between the $H\alpha$ VF in observations and Λ CDM simulations are selection effects in $H\alpha$ surveys, which are highly non-trivial to correct for. The latter is due to the fact that the typical galaxy with low circular velocity detected in ALFALFA is far from representative of galaxies of the same stellar or halo mass, particularly at $V_{\max} \lesssim 100 \text{ km s}^{-1}$, according to our predictions. The observed $H\alpha$ velocity distribution is therefore an excellent test for the baryon physics included in our cosmological galaxy formation models and simulations rather than a cosmological one.

A new generation of $H\alpha$ surveys is underway in telescopes such as The Australian Square Kilometer Array Pathfinder (ASKAP; Johnston et al. 2008). Examples of those are the Widefield ASKAP L-band Legacy All-sky Blind surveY (Staveley-Smith 2008) and the Deep Investigation of Neutral Gas Origins (Meyer 2009). The depth of these surveys will certainly lead to improvements over previous $H\alpha$ surveys; however, a careful consideration of systematic effects such as those described here will be necessary to make measurements that can be robustly compared with simulation predictions. Similarly, the exercise of simulating the selection effects of surveys to the detail presented here, will be equally important to identify the areas in which our understanding of galaxy formation and perhaps cosmology need improvement.

ACKNOWLEDGEMENTS

We thank Tom Quinn, Kristine Spekkens, Robin Cook, Barbara Catinella, Aaron Ludlow, Bi-Qing For, Jesus Zavala, Joop Schaye, and Marijn Franx for constructive comments and useful discussions. GC is funded by the MERAC Foundation, through the Postdoctoral Research Award of CL, and the University of Western Australia. We also thank Aaron Robotham and Rodrigo Tobar for their contribution towards SURFS and SHARK, and Mark Boulton for his IT help. Parts of this research were carried out by the ARC Centre of Excellence for All Sky Astrophysics in 3 Dimensions (ASTRO 3D), through project number CE170100013. CL and PE are funded by ASTRO 3D. KO received support from VICI grant 016.130.338 of the Netherlands Foundation for Scientific Research (NWO). This work was supported by resources provided by the Pawsey Supercomputing Centre with funding from the Australian Government and the Government of Western Australia.

REFERENCES

- Baugh C. M., 2006, *Rep. Prog. Phys.*, 69, 3101
 Baugh C. M. et al., 2019, *MNRAS*, 483, 4922
 Blitz L., Rosolowsky E., 2004, *ApJ*, 612, L29
 Blitz L., Rosolowsky E., 2006, *ApJ*, 650, 933
 Booth C. M., Schaye J., 2009, *MNRAS*, 398, 53
 Boylan-Kolchin M., Bullock J. S., Kaplinghat M., 2011, *MNRAS*, 415, L40
 Brooks A. M., Papastergis E., Christensen C. R., Governato F., Stilp A., Quinn T. R., Wadsley J., 2017, *ApJ*, 850, 97
 Bull P. et al., 2016, *Phys. Dark Universe*, 12, 56
 Bullock J. S., Boylan-Kolchin M., 2017, *ARA&A*, 55, 343
 Catinella B., Giovanelli R., Haynes M. P., 2006, *ApJ*, 640, 751
 Catinella B. et al., 2010a, *MNRAS*, 403, 683
 Catinella B. et al., 2010b, *MNRAS*, 403, 683
 Cole S., Lacey C., Baugh C., Frenk C., 2000, *MNRAS*, 319, 168
 Crain R. A. et al., 2015, *MNRAS*, 450, 1937
 Dalla Vecchia C., Schaye J., 2012, *MNRAS*, 426, 140
 Davies L. J. M. et al., 2018, *MNRAS*, 480, 768
 Duffy A. R., Schaye J., Kay S. T., Dalla Vecchia C., 2008, *MNRAS*, 390, L64
 Duffy A. R., Schaye J., Kay S. T., Vecchia C. D., Battye R. A., Booth C. M., 2010, *MNRAS*, 405, no
 Dutton A. A. et al., 2016, *MNRAS*, 461, 2658
 Dutton A. A., Macciò A. V., Buck T., Dixon K. L., Blank M., Obreja A., 2019, *MNRAS*, 486, 655
 Eckert K. D. et al., 2017, *ApJ*, 849, 20
 Elahi P. J., Welker C., Power C., Lagos C. d. P., Robotham A. S. G., Cañas R., Poulton R., 2018, *MNRAS*, 475, 5338
 Elahi P. J., Cañas R., Tobar R. J., Willis J. S., Lagos C. d. P., Power C., Robotham A. S. G., 2019a, *PASA*, 36, e021,
 Elahi P. J., Poulton R. J. J., Tobar R. J., Lagos C. d. P., Power C., Robotham A. S. G., 2019b, *PASA*, 36, e028,
 Elmegreen B. G., 1989, *ApJ*, 338, 178
 Fattah A. et al., 2016, *MNRAS*, 457, 844
 Fontanot F., Hirschmann M., De Lucia G., 2017, *ApJ*, 842, L14
 Giovanelli R. et al., 2005, *AJ*, 130, 2613
 Gonzalez A. H., Williams K. A., Bullock J. S., Kolatt T. S., Primack J. R., 2000, *ApJ*, 528, 145
 Haardt F., Madau P., 2001, in Neumann D. M., Tran J. T. V., eds, Clusters of Galaxies and the High Redshift Universe Observed in X-rays. Recontres de Moriond, Savoie, France, p. 64
 Hargis J. R., Willman B., Peter A. H. G., 2014, *ApJ*, 795, L13
 Haynes M. P. et al., 2018, *ApJ*, 861, 49
 Hopkins P. F., 2013, *MNRAS*, 428, 2840
 Johnston S. et al., 2008, *Exper. Astron.*, 22, 151
 Jones M. G., Haynes M. P., Giovanelli R., Moorman C., 2018, *MNRAS*, 477, 2
 Klypin A., Karachentsev I., Makarov D., Nasonova O., 2015, *MNRAS*, 454, 1798
 Komatsu E. et al., 2011, *ApJS*, 192, 18
 Kregel M., Van Der Kruit P. C., Grijl R. d., 2002, *MNRAS*, 334, 646
 Lacey C. G. et al., 2016, *MNRAS*, 462, 3854
 Lagos C. d. P. et al., 2014, *MNRAS*, 443, 1002
 Lagos C. d. P., Tobar R. J., Robotham A. S. G., Obreschkow D., Mitchell P. D., Power C., Elahi P. J., 2018, *MNRAS*, 481, 3573
 Leroy A. K., Walter F., Brinks E., Bigiel F., de Blok W. J. G., Madore B., Thornley M. D., 2008, *AJ*, 136, 2782
 Macciò A. V., Paduroiu S., Anderhalden D., Schneider A., Moore B., 2012, *MNRAS*, 424, 1105
 Macciò A. V., Udrescu S. M., Dutton A. A., Obreja A., Wang L., Stinson G. R., Kang X., 2016, *MNRAS*, 463, L69
 McGaugh S., 2012, *AJ*, 143, 40
 Merson A. I. et al., 2013, *MNRAS*, 429, 556
 Meyer M., 2009, in Panoramic Radio Astronomy: Wide-field 1-2 GHz Research on Galaxy Evolution, Proceedings of Science, Groningen, the Netherlands, p. 15
 Meyer M. J. et al., 2004, *MNRAS*, 350, 1195
 Navarro J. F., Frenk C. S., White S. D. M., 1995, *MNRAS*, 275, 720
 Obreschkow D., Croton D., De Lucia G., Khochfar S., Rawlings S., 2009, *ApJ*, 698, 1467
 Obreschkow D., Heywood I., Klöckner H. R., Rawlings S., 2009a, *ApJ*, 702, 1321
 Obreschkow D., Klöckner H. R., Heywood I., Levrier F., Rawlings S., 2009b, *ApJ*, 703, 1890
 Obreschkow D., Ma X., Meyer M., Power C., Zwaan M., Staveley-Smith L., Drinkwater M. J., 2013, *ApJ*, 766, 137
 Oman K. A. et al., 2015, *MNRAS*, 452, 3650
 Oman K. A., Marasco A., Navarro J. F., Frenk C. S., Schaye J., Benítez-Llambay A., 2019, *MNRAS*, 482, 821
 Papastergis E., Martin A. M., Giovanelli R., Haynes M. P., 2011, *ApJ*, 739, 38
 Papastergis E., Adams E. A. K., van der Hulst J. M., 2016, *A&A*, 593, A39
 Planck Collaboration XIII et al., 2016, *A&A*, 594, A13
 Plummer H. C., 1911, *MNRAS*, 71, 460
 Poulton R. J. J., Robotham A. S. G., Power C., Elahi P. J., 2018, *PASA*, 35, 42
 Rahmati A., Pawlik A. H., Raičević M., Schaye J., 2013, *MNRAS*, 430, 2427
 Rosas-Guevara Y. M. et al., 2015, *MNRAS*, 454, 1038
 Sales L. V. et al., 2017, *MNRAS*, 464, 2419
 Sawala T. et al., 2016, *MNRAS*, 457, 1931
 Schaller M., Dalla Vecchia C., Schaye J., Bower R. G., Theuns T., Crain R. A., Furlong M., McCarthy I. G., 2015, *MNRAS*, 454, 2277
 Schaye J., 2004, *ApJ*, 609, 667
 Schaye J., Dalla Vecchia C., 2008, *MNRAS*, 383, 1210
 Schaye J. et al., 2015, *MNRAS*, 446, 521
 Schneider A., Smith R. E., Macciò A. V., Moore B., 2012, *MNRAS*, 424, 684
 Schneider A., Trujillo-Gomez S., Papastergis E., Reed D. S., Lake G., 2017, *MNRAS*, 470, 1542
 Serra P. et al., 2010, in Verdes-Montenegro L., Del Olmo A., Sulentic J., eds, ASP Conf. Ser., Vol. 421, Galaxies in Isolation: Exploring Nature Versus Nurture. Astron. Soc. Pac., San Francisco, p. 49
 Springel V. et al., 2005, *Nature*, 435, 629
 Staveley-Smith L., 2008, *Astrophys. Space Sci. Proc.*, 5, 77
 Swaters R. A., Sancisi R., van Albada T. S., van der Hulst J. M., 2009, *A&A*, 493, 871
 Tollerud E. J., Bullock J. S., Strigari L. E., Willman B., 2008, *ApJ*, 688, 277
 Trujillo-Gomez S., Schneider A., Papastergis E., Reed D. S., Lake G., 2018, *MNRAS*, 475, 4825
 Tully R. B., Fisher J. R., 1977, *A&A*, 54, 661
 Walter F., Brinks E., de Blok W. J. G., Bigiel F., Kennicutt R. C., Thornley M. D., Leroy A., 2008, *AJ*, 136, 2563

- Wang L., Dutton A. A., Stinson G. S., Macciò A. V., Penzo C., Kang X., Keller B. W., Wadsley J., 2015, *MNRAS*, 454, 83
 Welker C., Power C., Lagos C. d. P., Elahi P. J., Cañas R., Pichon C., Dubois Y., 2018, *MNRAS*, 482, 2039
 Wiersma R. P. C., Schaye J., Theuns T., Dalla Vecchia C., Tornatore L., 2009, *MNRAS*, 399, 574
 Wiersma R. P. C., Schaye J., Smith B. D., 2009, *MNRAS*, 393, 99
 Zavala J., Jing Y. P., Faltenbacher A., Yepes G., Hoffman Y., Gottlöber S., Catinella B., 2009, *ApJ*, 700, 1779

- Zwaan M. A., Meyer M. J., Staveley-Smith L., Webster R. L., 2005, *MNRAS*, 359, 30

APPENDIX A: ASSESSMENT OF OUR H_I EMISSION-LINE MODEL AGAINST THE APOSTLE COSMOLOGICAL HYDRODYNAMICAL SIMULATIONS

The APOSTLE cosmological hydrodynamical simulations (Sawala

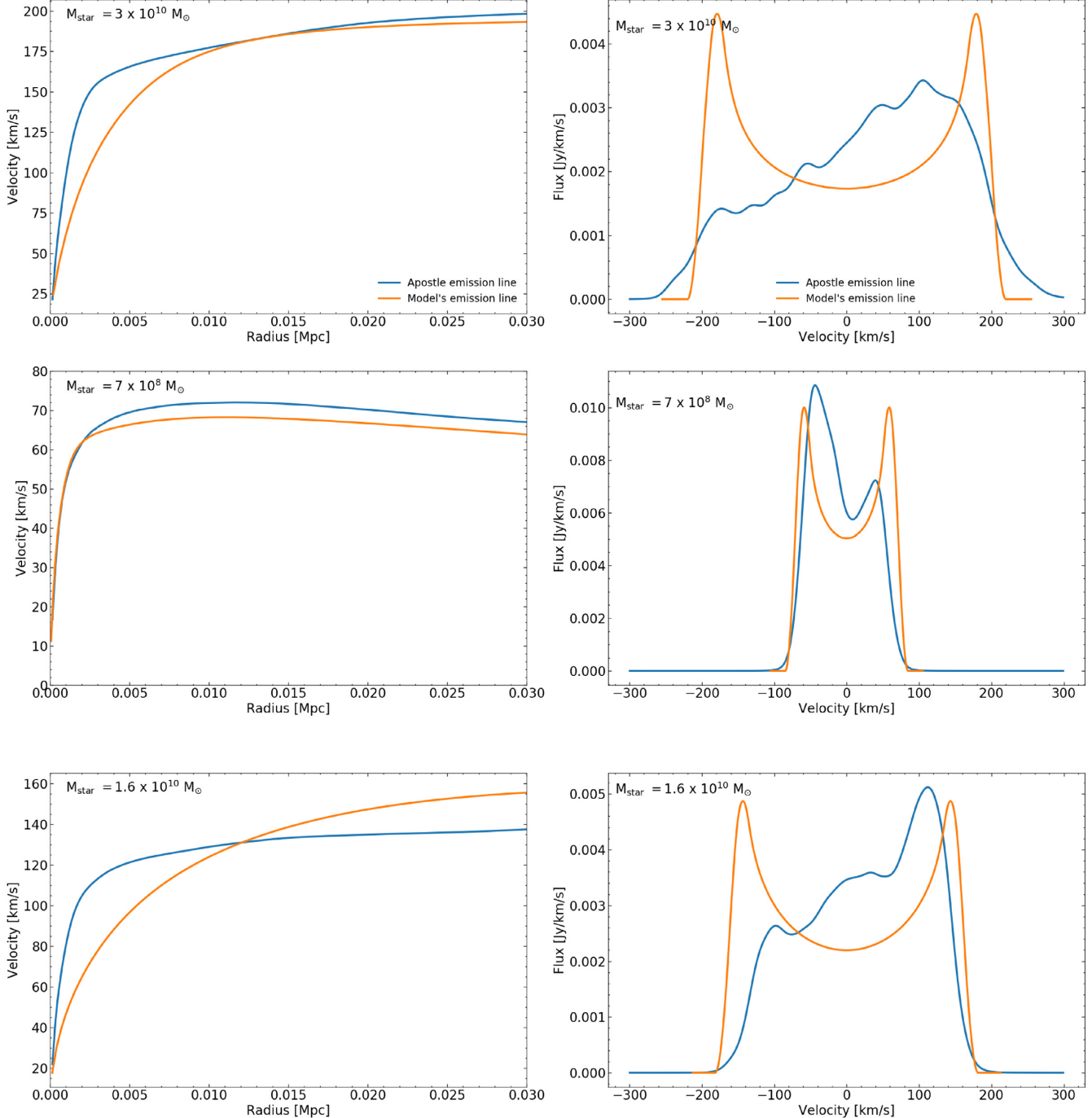


Figure A1. Rotational velocity curves (left-hand panel) and corresponding H_I emission-line profiles (right-hand panel) from the APOSTLE simulations compared to our model. The blue and orange lines correspond to APOSTLE and our model results, respectively, with the stellar mass of the galaxies as labelled. We show three examples of a galaxy in which our model does poorly (top panel), does well (middle), and an intermediate case (bottom).

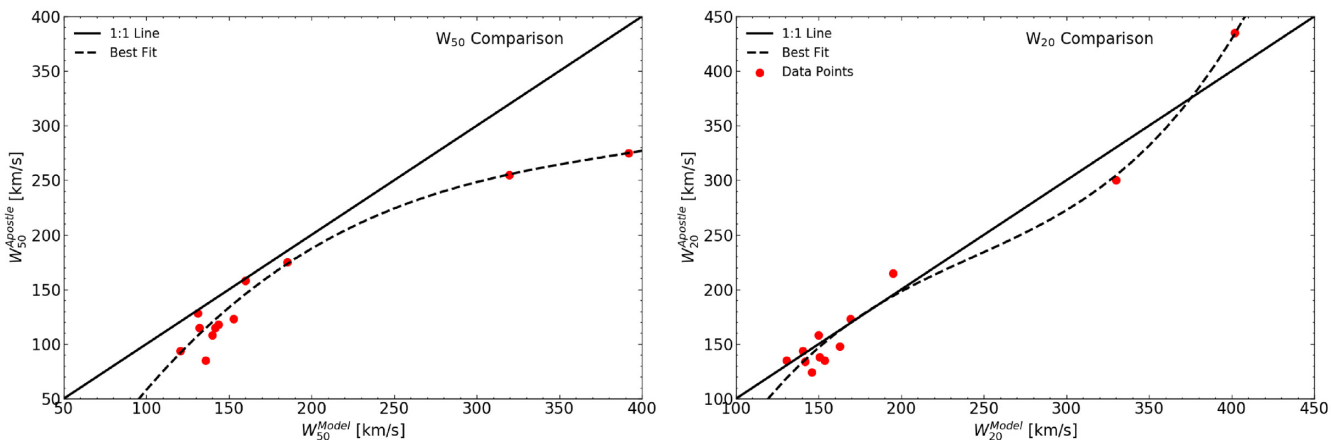


Figure A2. Comparison of the W_{20} and W_{50} measurements taken for the H I emission lines in APOSTLE and that produced by our idealized model, with the points being individual galaxies, the solid line being the 1:1 ratio and dashed line being the best spline fit. It should be noted that W_{20} measurements agree better between the hydrodynamical simulations and our idealized model than for W_{50} . This is because most of the H I emission-line spectra in APOSTLE are asymmetric, which affects W_{50} more than W_{20} .

et al. 2016) are a suite of 12 ‘zoom-in’ volumes evolved with the code and models developed and calibrated for the EAGLE project (Schaye et al. 2015; Crain et al. 2015). The volumes are selected to resemble the Local Group of galaxies in terms of the masses of two central objects – analogous to the MW and M31, their separation, relative velocity, and relative isolation from other massive systems. Each volume is evolved at three resolution levels. The lowest level L3 is similar to the fiducial EAGLE resolution (e.g. L0025N0376 in the nomenclature of Schaye et al. 2015), with a gas particle resolution of $\sim 10^6 M_\odot$ and gravitational softening of ~ 700 pc. The two higher resolution levels each decrease the particle resolution by a factor of ~ 8 , for a gas particle mass at maximum resolution L1 of $\sim 10^4 M_\odot$, and a gravitational softening of ~ 130 pc. The code uses the ANARCHY implementation (Schaller et al. 2015) of pressure–entropy smoothed particle hydrodynamics (Hopkins 2013), and includes prescriptions for radiative cooling (Wiersma, Schaye & Smith 2009), an ionizing background (Haardt & Madau 2001), SF (Schaye 2004; Schaye & Dalla Vecchia 2008), supernovae and stellar mass loss (Wiersma et al. 2009), energetic feedback from SF (Dalla Vecchia & Schaye 2012), and AGN (Booth & Schaye 2009; Rosas-Guevara et al. 2015). Full details of the model and calibration are available in Schaye et al. (2015) and Crain et al. (2015), and of the APOSTLE simulations in Sawala et al. (2016) and Fattahi et al. (2016). APOSTLE uses the REFERENCE calibration of the EAGLE model (see Schaye et al. 2015), and the WMAP7 cosmological parameters (Komatsu et al. 2011).

The code MARTINI² was used to produce neutral hydrogen (H I) emission-line profiles for a selection of galaxies from the APOSTLE simulations. A detailed description of an earlier version is available in Oman et al. (2019). The hydrogen ionization fraction of each simulation particle is estimated following Rahmati et al. (2013); the neutral hydrogen is further partitioned into atomic and molecular gas following Blitz & Rosolowsky (2006). Each particle contributes flux to the spectrum distributed as a Gaussian centred at the particle velocity, with a width specified by $\sqrt{k_B T/m_p}$, where k_B is Boltzmann’s constant, T is the particle temperature, and m_p is

the particle mass, and an amplitude proportional to the neutral hydrogen mass of the particle. The galaxies are placed edge-on ($i = 90^\circ$) at a fiducial distance of $D = 10$ Mpc, with a systemic velocity of $H_0 D$, with $H_0 = 70 \text{ km s}^{-1} \text{ Mpc}^{-1}$. The galaxies are selected morphologically to host gas discs, and to span a range in total (dynamical) mass, with 14 between $60 < V_{\max}/\text{km s}^{-1} < 120$ and 2 with $V_{\max} \sim 200 \text{ km s}^{-1}$, where V_{\max} is the maximum of the circular velocity curve. Other quantities required as inputs for our model were measured directly from the simulation particle properties – specifically, virial mass of the halo, H I, and stellar mass of galaxy and half-mass stellar and gas radii for the galaxy.

We build H I emission lines following the procedure described in Section 3 using the input global properties specified above. On the other hand, the H I emission lines from APOSTLE make full use of the complex geometry and non-circular motions that are predicted by the simulation. We compare our idealized model with the H I emission lines predicted by APOSTLE with the aim of understanding the systematic effects introduced by our assumptions with respect to more realistic H I line profiles. We used 13 dwarf galaxies and 2 MW-sized galaxies to compare our models.

In Fig. A1, we compare the H I emission for three example galaxies, highlighting cases in which our idealized model provided a poor and a good representation of the H I emission line (top and middle panels, respectively), with the bottom panel showing an intermediate case.

We find that for some galaxies the estimates of our model and the H I generated by the simulation show comparable widths and rotation curves but for others our model produces a rotation curve that flattens at smaller radii. When we compare the W_{50} and W_{20} (see Fig. A2), we notice that for galaxies with a higher mass or higher velocity and symmetric double-horned profile shape, we produce measurements that are close to the APOSTLE ones. We find better agreement in our W_{20} values than the W_{50} estimates. The cause for this is the asymmetry of the lines in the APOSTLE simulated galaxies, which leads to systematically different W_{50} estimates (due to the heights of the lines), which play a lesser role on W_{20} . This suggests that W_{20} should be a more stable, reliable estimate of the dynamical mass, in agreement with the inferences of McGaugh (2011).

²<https://github.com/kyleoman/martini>

The reason why the $\text{H}\alpha$ emission lines in APOSTLE are so asymmetric and whether that agrees with observations is unclear. Oman et al. (2019) studied the velocity profiles of APOSTLE dwarf galaxies, finding significant contribution from non-circular motions in addition to the purely circular velocity. Sales et al. (2017) found that APOSTLE dwarf galaxies may be significantly deviating from the measured Tully–Fisher relation of Papastergis, Adams & van der Hulst (2016). The latter may be an indication that feedback effects are too strong in APOSTLE. However, further research on the $\text{H}\alpha$ line profiles of APOSTLE galaxies is required before we can make draw robust conclusion.

Equations (A1) and (A2) show spline fits to the relations shown in Fig. A2. These equations could be used as an approximation to

the deviations of W_{50} and W_{20} from our idealized model.

$$\begin{aligned} W_{50\text{Apostle}} = & 6.02 \times 10^{-6} \times W_{50\text{Model}}^3 - 7.04 \times 10^{-3} \times W_{50\text{Model}}^2 \\ & + 2.98 \times W_{50\text{Model}} - 176.04 \end{aligned} \quad (\text{A1})$$

$$\begin{aligned} W_{20\text{Apostle}} = & 2.40 \times 10^{-5} \times W_{20\text{Model}}^3 - 1.75 \times 10^{-2} \times W_{20\text{Model}}^2 \\ & - 4.93 \times W_{20\text{Model}} - 280.69 \end{aligned} \quad (\text{A2})$$

This paper has been typeset from a $\text{\TeX}/\text{\LaTeX}$ file prepared by the author.